

Solid-state lighting—a benevolent technology

E Fred Schubert^{1,2,3}, Jong Kyu Kim^{1,2}, Hong Luo^{1,3} and J-Q Xi^{1,3}

¹ The Future Chips Constellation, Rensselaer Polytechnic Institute, 110 Eighth Street, Troy, NY 12180, USA

² Department of Electrical, Computer, and Systems Engineering, Rensselaer Polytechnic Institute, 110 Eighth Street, Troy, NY 12180, USA

³ Department of Physics, Applied Physics, and Astronomy, Rensselaer Polytechnic Institute, 110 Eighth Street, Troy, NY 12180, USA

E-mail: EFSchubert@rpi.edu

Received 6 July 2006

Published 2 November 2006

Online at stacks.iop.org/RoPP/69/3069

Abstract

Solid-state light sources are in the process of profoundly changing the way humans generate light for general lighting applications. Solid-state light sources possess two highly desirable features, which set them apart from most other light sources: (i) they have the potential to create light with essentially unit power efficiency and (ii) the properties of light, such as spectral composition and temporal modulation, can be controlled to a degree that is not possible with conventional light sources such as incandescent and fluorescent lamps. The implications are enormous and, as a consequence, many positive developments are to be expected including a reduction in global energy consumption, reduction of global-warming-gas and pollutant emissions and a multitude of new functionalities benefiting numerous applications. This review will assess the impact of solid-state lighting technology on energy consumption, the environment and on emerging application fields that make use of the controllability afforded by solid-state sources. The review will also discuss technical areas that fuel continued progress in solid-state lighting. Specifically, we will review the use of novel phosphor distributions in white light-emitting diodes (LEDs) and show the strong influence of phosphor distribution on efficiency. We will also review the use of reflectors in LEDs with emphasis on ‘perfect’ reflectors, i.e. reflectors with highly reflective omni-directional characteristics. Finally, we will discuss a new class of thin-film materials with an unprecedented low refractive index. Such low- n materials may strongly contribute to the continuous progress in solid-state lighting.

(Some figures in this article are in colour only in the electronic version)

This article was invited by Professor K Ploog.

Contents

	Page
1. Benefits of solid-state lighting	3071
1.1. Introduction to solid-state lighting	3071
1.2. Theoretical limits for efficiency	3071
1.3. Potential savings in energy and reduction of environmental pollution	3072
1.4. Solid-state lighting—beyond energy	3075
2. Highly efficient packaging configurations for phosphor-based white LED lamps	3076
2.1. Phosphor configurations in white LED lamps	3076
2.2. Whispering-gallery modes and diffuse reflector cups	3077
2.3. Simulation and experiment of phosphorescence efficiency	3080
3. Omni-directional reflectors for light-emitting diodes	3083
3.1. Reflectors for light-emitting diodes	3083
3.2. GaInN blue light-emitting diodes with omni-directional reflectors	3085
3.3. GaInN near ultraviolet light-emitting diodes with omni-directional reflectors	3089
3.4. AlGaInP light-emitting diodes with omni-directional reflectors	3091
4. Low-refractive-index optical thin films and their applications	3092
4.1. Low-refractive-index materials	3092
4.2. Oblique-angle deposition for films consisting of an array of nano-rods	3093
4.3. Low-refractive-index SiO ₂	3094
4.4. Optical multilayer structure with low-refractive-index SiO ₂ thin film	3095
5. Conclusions	3097
Acknowledgments	3098
References	3098

1. Benefits of solid-state lighting

1.1. Introduction to solid-state lighting

The very first solid-state light source was demonstrated approximately 100 years ago by Henry J Round, a radio engineer who was searching for better crystal detectors for radio waves, when he accidentally discovered that light was being emitted from a man-made SiC crystal when a current flowed through the material. He saw a remarkably broad range of colours including orange, yellow, green and blue. Over the last century, remarkable progress has been made in solid-state light-emitting devices, most particularly during the last 50 years. At the present time, technical advances in solid-state light sources are continuing unabated with sources continuously becoming more powerful, brighter and more efficient.

A new era is dawning, the era of solid-state lighting in which the technical community has reason to believe that solid-state lighting will develop into a benevolent technology that will benefit humanity at large.

Three major benefits of solid-state lighting technology, shown in figure 1, can be summarized as follows: *firstly*, the inherent capability of solid-state sources to generate light with high efficiency is resulting in giant energy savings. *Secondly*, potentially huge environmental benefits are a result of the efficiency and durability of solid-state emitters, particularly light-emitting diodes based on inorganic semiconductors. *Thirdly*, solid-state emitters allow one to control the emission properties with much greater precision, thereby allowing one to custom-tailor the emission properties for specific applications. Next, these benefits will be discussed quantitatively and in detail.

1.2. Theoretical limits for efficiency

An exciting aspect of solid-state lighting is the availability of several types of efficient solid-state sources that emit high-quality white light. Solid-state lighting systems can be categorized into *dichromatic* and *trichromatic* approaches, and independently, into systems that are based on active (i.e. current-injected) emitters and non-current-injected phosphor wavelength-converters. The resulting four basic approaches are shown in figure 2. In addition to these approaches, approaches for higher chromaticity (e.g. tetra-chromatic approaches) and mixed approaches (e.g. two types of LEDs and one phosphor) are possible. Which of these approaches is the best and which will become dominant in the marketplace? At this time, the winning technology is not yet known. There is a general belief that phosphors will be part of simple, small-scale solid-state lighting systems. There is also the belief that efficient green emitters will be needed for systems based on LEDs. But only time will tell the specific technology that future solid-state lighting systems will be based upon.

There are a number of considerations that distinguish the different approaches. We summarize the advantages and disadvantages as follows.

- The luminous efficacy of radiation (i.e. luminous flux divided by optical power, measured in units of lm W^{-1}) is highest for dichromatic sources and generally decreases with the number of sources, i.e. the degree of poly-chromaticity. The luminous efficacy of dichromatic, trichromatic and tetra-chromatic sources can exceed 400 lm W^{-1} , 300 lm W^{-1} and 275 lm W^{-1} , respectively. At these efficacies, both tri-chromatic and tetra-chromatic sources have very reasonable colour-rendering properties. Colour-rendering indices greater than 90 have been reported for such sources [1].
- Let us assume that a solid-state source is purely based on current-injected devices and contains no phosphors, and let us further assume that the devices have a 100%

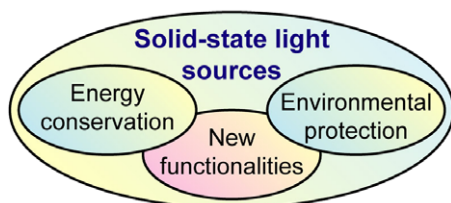


Figure 1. Benefits enabled by solid-state light sources.

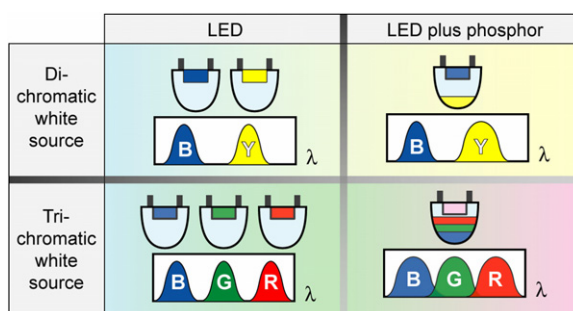


Figure 2. Approaches to solid-state lighting sources for general lighting applications.

electrical-to-optical-power-conversion efficiency. Then the luminous efficacy of radiation is equal to the luminous source efficiency (i.e. luminous flux divided by electrical input power, measured in units of lm W^{-1} as well).

- Devices containing phosphor wavelength-converters have advantages such as simplicity, colour stability and the need for only one power source. However, devices containing phosphors generally have a lower efficiency because of the unavoidable energy loss concomitant with the wavelength-conversion of a photon from wavelength λ_1 to λ_2 with $\lambda_2 > \lambda_1$. The energy loss is particularly large for wavelength-conversion processes from the UV (400 nm) to the red (625 nm) where the loss is 36%.
- It is reasonable to assume that, given sufficient time and resources for development, the goal of reaching 50% of the theoretical maximum of the luminous efficiency is reasonable with a very good chance of being reached. Thus a luminous efficiency of 50% of 300 lm W^{-1} , i.e. 150 lm W^{-1} , is an optimistic yet reasonable long-term expectation for commercial solid-state sources emitting high-quality white light.

There are many other aspects of solid-state devices that are highly relevant including the internal quantum efficiency of the active region, light-extraction, current-flow design, the minimization of resistive losses, electrostatic discharge stability, reliability, scalability to increase the luminous flux per LED package and a low purchase price, to just name a few. A comprehensive discussion of these important factors is not the intent of the authors and the reader is referred to the literature for a detailed discussion of these topics [2].

1.3. Potential savings in energy and reduction of environmental pollution

The total annual production of electrical energy in the US in 2004 was $14.98 \times 10^{18} \text{ J} = 4161 \text{ TWh} = 14.20 \times 10^{15} \text{ BTU}$ [3]. The US Department of Energy estimates that 22% of electricity is used for lighting [5]. Thus, the electrical energy generated annually in the

Table 1. Annual energy expended by end users in US on different lighting sources, their luminous source efficiency and luminous flux multiplied by operating time [5]. The weighted average of the luminous efficiency of all sources is 56.09 lm W^{-1} .

	Annual electrical energy consumed in US for lighting (TWh)	Luminous efficiency (lm W^{-1})	Luminous flux \times time (Tlmh = Tera lumen hr)
Incandescent	321	$\times 15$	$= 4\ 815$
Fluorescent	313	$\times 80$	$= 25\ 040$
High-intensity discharge	130	$\times 100$	$= 13\ 000$
Total	764 ^(a)	56.09 (weighted average)	42 855

^a Note that 764 TWh does not include transmission, distribution and other losses, whereas 915.4 TWh, cited in the text, does.

US for lighting is 915.4 TWh [3]. Note that this number, 915.4 TWh, includes electricity for power-plant use as well as transmission and distribution losses, the sum of which is estimated at 14.01% [3]. Earlier technical discussions of potential energy savings resulting from solid-state lighting were given by Bergh *et al* [4].

At present, light sources used for general lighting include incandescent light bulbs, fluorescent sources and high-intensity discharge sources. The annual consumption of electrical energy by these sources is given in table 1 [5]. The 4th row of table 1 contains the sum of the annual energies expended in the US on lighting and the sum of the luminous flux \times operating time of all light sources for one year. These two quantities allow us to calculate the *luminous efficiency of a hypothetical average light source*; it is 56.09 lm W^{-1} . Assuming that new solid-state sources will have a luminous efficiency of 150 lm W^{-1} , energy savings will materialize as more and more conventional light sources are replaced by power-saving solid-state sources.

For a 0% market penetration of solid-state lighting technology, a power of $56.09^{-1} \text{ W} = 0.01783 \text{ W}$ would be needed to generate 1 lm.

For a 40% market penetration of solid-state lighting technology, a power of $(6/10)56.09^{-1} \text{ W} + (4/10)150^{-1} \text{ W} = 0.013\ 36 \text{ W}$ would be needed to generate 1 lm. This represents an energy saving of about 25% (to be exact 25.05%) over the 0% penetration scenario. Thus the total electricity consumption could be reduced by 5.5% and we will refer to this as the ‘5.5% scenario’ in our following considerations. The potential annual electrical energy savings would amount to 228.9 TWh or 5.5% of the overall electrical energy currently generated in the US annually, i.e. one quarter of the electrical energy currently used for lighting in the US per year.

For an 80% market penetration of solid-state lighting technology, a power of $(2/10)56.09^{-1} \text{ W} + (8/10)150^{-1} \text{ W} = 0.008899 \text{ W}$ would be needed to generate 1 lm. This represents an energy saving of about 50% (to be exact 50.09%) over the 0% penetration scenario. Thus the total electricity consumption could be reduced by 11% and we will refer to this as the ‘11% scenario’ in our following considerations. In this more optimistic scenario, the potential energy savings are estimated to be 457.8 TWh or 11% of the total electrical energy generated in the US annually, i.e. one half of the electrical energy currently used for lighting in the US per year.

Financial savings follow directly from the electrical energy savings. Assuming that 1 kWh costs \$0.10, the annual US financial savings would be \$22.89 billion for the 5.5% scenario. In the more optimistic 11% scenario, annual US financial savings would be \$45.78 billion.

Gigantic and very positive environmental effects accompany the electrical energy savings. Assuming that the average efficiency of energy conversion of all electricity-generating power plants is 34.83% [3], the annual input energy of power plants is $43.01 \times 10^{18} \text{ J}$. Of this energy, 69.29% or $29.80 \times 10^{18} \text{ J}$ is generated as heat energy by fossil-fuel burning power plants [3].

Of the fossil-fuel burning plants 72.85% of the heat energy is produced by coal-burning plants, 22.62% by gas-burning plants and 4.53% by oil-burning plants. Whereas coal (i.e. mostly carbon), when burning, is completely converted to the global-warming gas CO₂, oil and natural gas contain hydrogen, so that the thermal power is derived from both the oxidation of carbon as well as the oxidation of hydrogen.

Next we restrict our considerations to coal-burning power plants. The heat energy created annually by coal-burning power plants in the US is thus $29.80 \times 10^{18} \text{ J} \times 72.85\% = 21.71 \times 10^{18} \text{ J}$. Upon burning, carbon creates heat energy that is quantified as

$$1 \text{ kg of C creates heat energy of } 32.80 \times 10^6 \text{ J during reaction } \text{C} + \text{O}_2 \rightarrow \text{CO}_2. \quad (1)$$

Thus the mass of carbon burned annually in the US by coal-burning power plants is given by $21.71 \times 10^{18} \text{ J} / (32.80 \times 10^6 \text{ J kg}^{-1}) = 661.9 \times 10^9 \text{ kg} = 661.9 \text{ Mt}$ (megatons). Upon oxidation, one carbon atom with 12 amu (atomic mass units) reacts with two oxygen atoms with oxygen having 16 amu. Thus 1 kg of carbon creates $(12 \text{ amu} + 2 \times 16 \text{ amu}) / (12 \text{ amu}) \text{ kg} = 3.667 \text{ kg}$ of CO₂.

$$1 \text{ kg of carbon, upon burning, creates } 3.667 \text{ kg of CO}_2. \quad (2)$$

Thus the 661.9 Mt of carbon burned annually in the US in electricity-generating power plants generates 2427 Mt of the green-house gas CO₂. Taking the above derived projected energy savings of the 5.5% scenario, the potential reduction in CO₂ emission would be 133.5 Mt per year in the US. Taking the above derived more optimistic energy savings of the 11% scenario, the potential reduction in CO₂ emission would be 267.0 Mt per year in the US.

Note that CO₂ is also being generated by oil and natural-gas burning power plants. These CO₂ emissions have not been considered above. Thus, the amount of CO₂ calculated above is again a very conservative estimate.

The electrical energy generated annually in the US is 4161 TWh. This energy corresponds to an average power of $4161 \text{ TWh} / (365.25 \times 24 \text{ h}) = 475 \text{ GW}$. A reduction of power consumption in the 5.5% scenario would alleviate the need to generate 26.13 GW or the need for 35 major power stations each of which is assumed to generate approximately 750 MW. The more optimistic 11% scenario would alleviate the need to generate 52.26 GW or the need for 70 major power stations.

As mentioned above, $29.80 \times 10^{18} \text{ J}$ in heat energy is produced annually in the US by fossil-fuel burning power plants. Since 4.53% of the heat energy is produced by oil-burning plants, they produce a heat energy of annually $29.80 \times 10^{18} \text{ J} \times 4.53\% = 1.350 \times 10^{18} \text{ J}$. One barrel of crude oil (159 litres) generates a heat energy of $6.170 \times 10^9 \text{ J}$ ($= 5.848 \times 10^6 \text{ BTU}$).

$$\text{One barrel of crude oil, upon burning, generates a heat energy of } 6.170 \times 10^9 \text{ J}. \quad (3)$$

Thus, oil-burning power plants are using 218.8×10^6 barrels of oil per year in the US. The introduction of solid-state lighting technology would alleviate the need for 12.03×10^6 and 24.07×10^6 barrels of oil per year in the US in the 5.5% and 11% scenario, respectively.

The potential savings can be extrapolated to a global scenario, by taking into account that the US is consuming about one quarter (1/4) of the world's energy [6]. In a global scenario, the expected savings over a period of 10 years are listed in table 2. Inspection of the data of table 2 shows that the anticipated energy savings are truly breathtaking. Solid-state lighting technology is becoming a global technology with the true winner being the planet Earth and all her inhabitants.

It is understood that a number of approximations have been made in the above considerations including the negligence of growth rates, inflation and national differences in the

Table 2. Global benefits enabled by solid-state lighting technology over a period of 10 years. The first numeric value in each box of the table represents the annual US numeric value. The US uses about 1/4 of the world's energy.

	Savings under '5.5% scenario'	Savings under '11% scenario'
Reduction in total energy consumption	$43.01 \times 10^{18} \text{ J} \times 5.5\% \times 4 \times 10$ $= 94.62 \times 10^{18} \text{ J}$	$43.01 \times 10^{18} \text{ J} \times 11\% \times 4 \times 10$ $= 189.2 \times 10^{18} \text{ J}$
Reduction in electrical energy consumption	$228.9 \text{ TWh} \times 4 \times 10 = 9,156 \text{ TWh}$ $= 32.96 \times 10^{18} \text{ J}$	$457.8 \text{ TWh} \times 4 \times 10 = 18,310 \text{ TWh}$ $= 65.92 \times 10^{18} \text{ J}$
Financial savings	$22.89 \times 10^9 \$ \times 4 \times 10 = 915.6 \times 10^9 \$$	$45.78 \times 10^9 \$ \times 4 \times 10 = 1,831 \times 10^9 \$$
Reduction in CO ₂ emission	$133.5 \text{ Mt} \times 4 \times 10 = 5.340 \text{ Gt}$	$267.0 \text{ Mt} \times 4 \times 10 = 10.68 \text{ Gt}$
Reduction of crude-oil consumption	$12.03 \times 10^6 \text{ barrels} \times 4 \times 10$ $= 481.2 \times 10^6 \text{ barrels}$	$24.07 \times 10^6 \text{ barrels} \times 4 \times 10$ $= 962.4 \times 10^6 \text{ barrels}$
Number of power plants not needed	$35 \times 4 = 140$	$70 \times 4 = 280$

cost of electricity. Nevertheless the strong benefit of the above calculation is its transparency that is not easily given in more complex models, particularly in models that are based on non-analytical numerical computations.

In addition to energy savings and reductions in global-warming-gas emissions, positive environmental effects can be summarized as follows: *firstly*, in contrast to fluorescent light sources, solid-state light sources do not contain mercury. Thus a strong reduction of mercury coming from fluorescent lamps in homes and offices will result from the introduction of solid-state sources. *Secondly*, a strong reduction of acid-rain-causing SO₂, mercury, radio-active materials and other pollutants that are known to be emitted by coal-burning power plants, is to be expected from the introduction of solid-state sources.

The energy-saving benefits of solid-state lighting technology have already materialized in numerous applications, one of the most widely discussed being traffic lights. For such monochromatic red, yellow or green lights, energy savings are particularly large because in the past the colours were generated by filtering out the unwanted spectral regions of the light emitted from a white incandescent source. Solid-state sources have allowed the energy consumption of traffic lights to be reduced by about one order of magnitude.

1.4. Solid-state lighting—beyond energy

Solid-state lighting has yet another dimension: solid-state light sources can be controlled and real-time tuned in terms of a number of characteristics that are shown in figure 3. The controllable properties include the spectral composition, polarization, colour temperature, temporal modulation and far-field pattern, thereby enabling paradigmatic shifts in multiple application areas such as imaging and biotechnology, human health, transportation, communications, agriculture, display technology and general lighting.

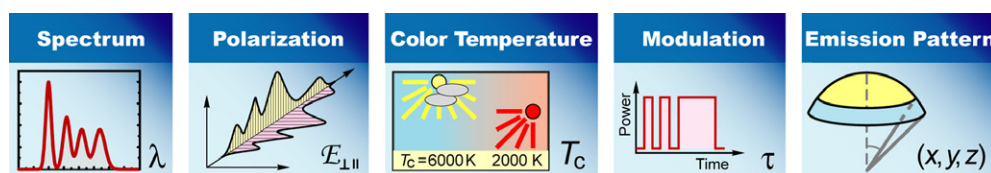


Figure 3. Characteristics of solid-state light sources that, in contrast to conventional lighting sources, can be controlled and tuned with high accuracy.

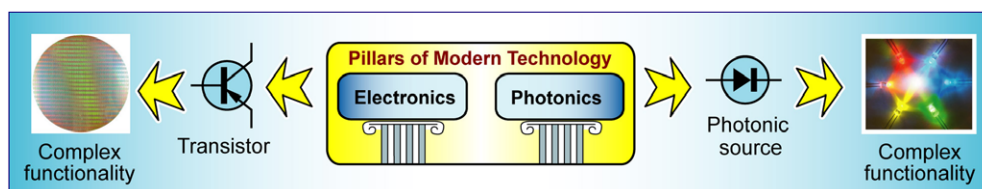


Figure 4. Vision for the future development of photonic sources and analogy with electronics.

Our long-term vision is illustrated in figure 4, which shows two major pillars of modern technology: electronics and photonics. The transistor, the key element of electronics, was initially intended to replace the triode vacuum tube. However, the complex functionality afforded by integrated circuits has sparked an enormous, still ongoing, revolution. The key element of photonics, the solid-state light source, is intended to replace conventional incandescent light bulbs and fluorescent sources. However, we anticipate that the increased functionality afforded by solid-state sources will spark an enormous revolution.

The ability to custom-tailor solid-state sources for specific applications could have dramatic long-term benefits [1].

- **Imaging and biology.** Advances in quantitative biology, particularly the rapid identification and counting of biological cells through adaptive and fully tunable reflectance and fluorescence imaging [7, 8].
- **Human health.** Reduced dependence on sleep-inducing pharmaceuticals, higher productivity, the prevention of certain cancers [9, 10] and higher quality of life.
- **Transportation.** Enhanced safety and visibility through communicating headlights and brake lights, interactive roadways and headlamps with dispersive characteristics adapted to the different spectral sensitivities of central and peripheral vision [11].
- **Communications.** Fundamentally new modes of broadcasting, communications and sensing through temporal control of room-lighting sources [12].
- **Agriculture.** Efficient plant growth in non-native seasons and regions (including outer space) [13].
- **Displays.** Liquid-crystal-based TVs, monitors, displays and projectors with unprecedented efficiency and brilliance (huge colour gamut) through polarized sources [14].

In order to make these benefits become reality, great advances will be needed in solid-state light-emitter technology. These advances include the availability of highly efficient sources across the visible spectrum and the ultraviolet range, the scalability of devices without scaling-induced losses and low cost. In the remainder of this review we will select a few specific topics that we believe have the potential to greatly advance solid-state lighting technology. The selection of topics is by no means comprehensive. It is rather a selection of topics with which the authors have familiarity and have made technical contributions to.

2. Highly efficient packaging configurations for phosphor-based white LED lamps

2.1. Phosphor configurations in white LED lamps

For phosphor-based white LEDs, the phosphor absorbs the short-wavelength emission from the primary LED chip and down-converts it to a longer-wavelength emission. For example, the first phosphor-based white LED used a blue GaInN LED pumping a YAG:Ce³⁺ yellow phosphor [15]. The phosphor density and thickness is chosen to transmit only a fraction of the

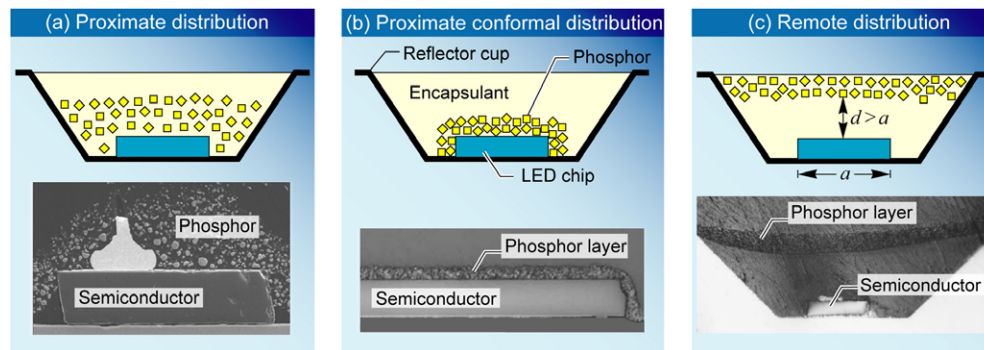


Figure 5. Phosphor placements in LED lamps. (a) Proximate phosphor-in-cup distribution [16]. (b) Proximate conformal phosphor distribution [16]. (c) Remote phosphor distribution [17, 18].

blue light. Mixing yellow phosphorescence with the blue electroluminescence results in white light. The amount, density and distribution of phosphor inside LED packages are adjusted to optimize the colour-rendering characteristics and the device efficiency.

The placement and arrangement of phosphors are critical for both the luminous source efficiency and colour rendering index of the white LED lamps. Typical arrangements of phosphor in white LED lamps are shown in figure 5. The first generation white LEDs are fabricated by dispensing the phosphor into epoxy within a reflector cup. We refer to this configuration as *proximate phosphor-in-cup distribution*, as shown in figure 5(a). For this process, it is difficult to control the uniformity of the phosphor distribution and the phosphor grain size variation, which, for non-uniform distributions, will result in colour variation for different view angles. Figure 5(b) shows another *proximate* phosphor distribution, in which the phosphor layer *conformally* coats the LED chip. In this case, the colour variation at different viewing angles is reduced dramatically due to the thickness uniformity of the phosphor layer, which provides the blue emission with an equal optical path length in the phosphor material, independent of the emission direction [16]. For both phosphor-in-cup and conformal phosphor distributions, phosphors are closely distributed around the LED chip. Because the phosphorescence emission is isotropic, a large portion of the light emitted from phosphor directly impinges on the LED chip. The contacts and bonding metals of the LED chip are absorptive at the phosphorescence wavelength [19]. This issue is especially severe in conformal phosphor distribution due to the close proximity between the phosphor and the absorptive LED chip.

Placing the phosphor layer at a sufficiently large distance from the LED chip, as shown in figure 5(c), reduces the probability of the phosphorescence directly hitting the chip. The phosphor forms a uniform layer on the top of the reflector cup, which we refer to as *remote phosphor* [17, 18]. The thickness of the remote phosphor can be well controlled, which results in excellent colour uniformity. In addition, the separation of phosphor from the LED chip reduces the operating temperature for phosphor, which in turn is expected to improve the lamp lifetime.

2.2. Whispering-gallery modes and diffuse reflector cups

Most of the metal reflector cups employed in LED packages have a truncated-cone shape for reflecting the LED emission towards the top and out of the package. For white LED

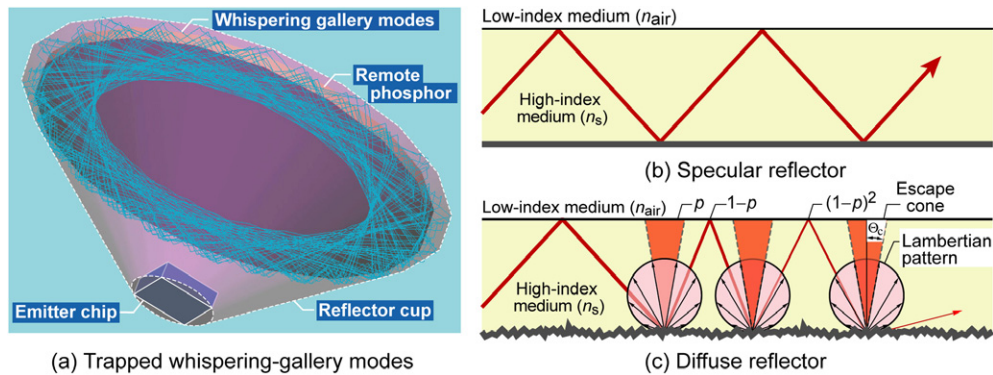


Figure 6. (a) Trace of a single ray inside the LED lamp with remote phosphor, illustrating a trapped whispering-gallery mode (after Luo *et al* [21]). (b) Optical mode guided by specular reflector and the semiconductor/air interface. (c) Reflector with a diffuse reflection component, as well as a specular reflection component. Diffuse reflection can redirect guided modes into an escape cone.

lamps, the cup is Ag-coated, taking advantage of the high reflectivity of Ag in the visible wavelength range. Because of the high symmetry of the reflector cup and encapsulant dome, trapped optical modes can occur in LED packages, as shown in figure 6(a). In these trapped modes, light propagates along the circumference of the encapsulant, reminiscent of *whispering-gallery modes*, which are optical modes confined by multiple total internal reflections. The term ‘whispering-gallery modes’ [20] was first defined by Lord Rayleigh in 1912 to describe the phenomenon of acoustic waves propagating around the interior gallery of Saint Paul’s Cathedral in London, England. For whispering-gallery modes in LED packages, multiple reflections occur on the reflector-cup/encapsulant and encapsulant/air interfaces, as shown in figure 6. Assuming an Ag-coated reflector cup with reflectivity of 95%, the power of a light ray decreases to 60% of its original value after only 10 Ag reflection events, indicating that the whispering-gallery modes inside the package are a significant loss mechanism.

To eliminate the trapped modes, non-deterministic components need to be included in LED packages, such as a *diffuse* reflector cup, a *textured* encapsulant dome or a mineral *diffuser* (e.g. ground glass) that is added to the encapsulant. These non-deterministic components introduce chaotic optical processes, i.e. diffuse reflections or scattering, which reduce the number of trapped whispering-gallery modes and enhance light extraction. Here, we concentrate on LED packages that employ a diffuse reflector cup.

For a specular reflector cup, the angle of reflectance equals the angle of incidence. Due to total internal reflection, light is trapped inside the high index medium and its energy finally dissipates in multiple reflections, as shown in figure 6(b). For a diffuse reflector cup, the diffusely reflected light I has a Lambertian distribution with an intensity $I \propto \cos \theta$ [22], irrespective of the incidence angle, where θ is the reflection angle with respect to the surface normal, as shown in figure 6(c). Every diffuse reflection provides a probability p for the light to escape into free space, thereby reducing the multiple-reflection losses. A reflective surface with surface irregularities that are in size comparable to or greater than the wavelength of light, which can be achieved by surface roughening, reflects light diffusely. However, real surface-roughened reflectors almost always have a *diffuse* as well as a *specular* reflection component. We refer to such reflectors as *partially diffuse reflectors*. To investigate the influence of a partially diffuse reflector cup on the phosphorescence efficiency, it is desirable to quantify the specularity and diffusivity of roughened reflector cups. The reflectance pattern of a diffuse

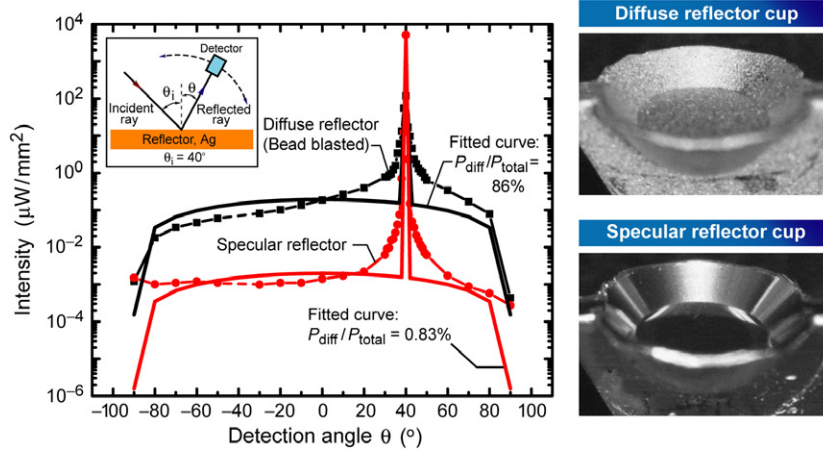


Figure 7. Measured angular dependence of reflectivity for a specular (i.e. smooth) and a diffuse (i.e. roughened by bead blasting) Ag reflector. Fitting the experimental data to the theoretical model gives a diffuse-to-total-reflected-power ratio of 0.83% and 86% for the specular and diffuse Ag reflectors, respectively. Also shown are photos of the two Ag reflector cups.

reflector can be described by [23]:

$$I(\theta, \phi) = I_{\text{diff}} \cos(\theta) + I_{\text{spec}} \cos(\theta) \frac{1}{\sigma^2 2\pi} \exp\left[-\frac{1}{2} \left(\frac{\theta - \theta_i}{\sigma}\right)^2\right] \exp\left[-\frac{1}{2} \left(\frac{\phi - \phi_i}{\sigma}\right)^2\right], \quad (4)$$

where ϕ and θ are the azimuthal and polar angle of reflectance and ϕ_i and θ_i are the azimuthal and polar angle of incidence, respectively. I_{diff} is the maximum intensity for diffuse reflection, and $I_{\text{spec}} \cos(\theta_i) / (\sigma^2 2\pi)$ is the maximum intensity for specular reflection. The diffuse reflection intensity, given by the first summand on the right-hand side of equation (4), follows the Lambertian distribution. The second summand describes the specular reflection intensity, which is assumed to be broadened as a Gaussian function. Fitting equation (4) to measured angular dependent reflectivity data of a partially diffuse reflector will give us I_{diff} , I_{spec} and σ . The diffuse and specular reflection power (P_{diff} and P_{spec}) are then obtained by integrating the first and second summand of the equation over space, i.e. over $0^\circ \leq \theta \leq 90^\circ$ and $0^\circ \leq \phi \leq 180^\circ$. The diffusivity and specularity are then determined by the equations

$$\text{diffusivity} = P_{\text{diff}} / (P_{\text{diff}} + P_{\text{spec}}), \quad (5)$$

$$\text{specularity} = P_{\text{spec}} / (P_{\text{diff}} + P_{\text{spec}}). \quad (6)$$

To investigate the angular dependent reflectivity of specular and diffuse reflector cups, a smooth and a bead-blasted Ag reflector are fabricated and measured using a He–Ne laser emitting at 632 nm. The incident angle is 40° and the reflected light intensity is measured from -90° to 90° , as shown in the inset of figure 7. Compared with the specular reflector, the diffuse reflector shows a *two orders of magnitude* higher diffusely reflected power. Fitting equation (4) to the experimental data gives a diffusivity of 86% for the bead-blasted Ag reflector and of 0.83% for the specular Ag reflector. Photos of Ag coated specular and diffuse reflector cups are also shown in figure 7.

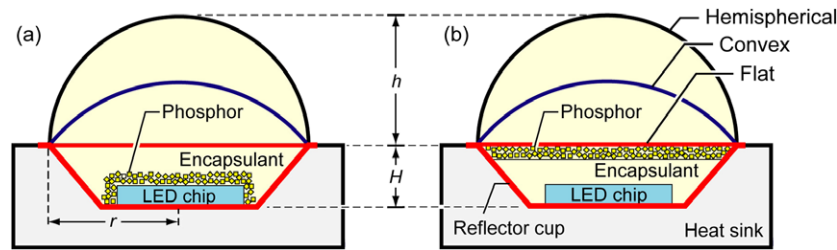


Figure 8. Cross-sectional view of the dichromatic white LED lamps with (a) proximate and (b) remote phosphor distribution. Three different geometries of the encapsulation dome, flat ($h = 0$), convex ($h = r/2$) and hemispherical ($h = r$), are shown.

2.3. Simulation and experiment of phosphorescence efficiency

Ray tracing simulation is a powerful tool for predicting the light extraction efficiency of LED lamps. Three-dimensional ray tracing simulations are performed for different LED lamp structures shown in figure 8. In the packages, a truncated-cone shaped reflector cup is filled with an encapsulant with a refractive index of $n_{\text{encapsulant}} = 1.6$. A square-shaped $1 \times 1 \text{ mm}^2$ LED chip with thickness of $300 \mu\text{m}$ is located at the bottom centre of the cup. At phosphorescence wavelength ($\lambda = 550 \text{ nm}$), the reflectance of the chip is assumed to be 50% ($R_{\text{LED chip}} = 50\%$). The bottom diameter of the reflector cup is 1.4 mm . The sidewall angle θ_s is 45° . The cup height H is varied in the simulations. The reflector cup can be either specular, diffuse or partially diffuse. For both the specular cup and diffuse cup, the overall reflectance of the cup is 95% ($R_{\text{reflector}} = 95\%$). A uniform cylindrical light source with thickness of $100 \mu\text{m}$ is immersed into the encapsulant, representing the phosphor layer emitting at 550 nm .

Two different phosphor arrangements, namely a *proximate* and a *remote* phosphor configuration, are simulated. For the proximate phosphor arrangement, the phosphor layer is placed conformally on the LED chip. For the remote phosphor arrangement, the phosphor layer is placed at the top of the reflector cup. Both the encapsulant and phosphor are transparent at 550 nm . Scattering by the phosphor can be neglected in the simulations for two idealized cases: (i) a small or negligible difference between the refractive index of the phosphor and the encapsulant; (ii) for nano-phosphors in which the phosphor-particle size is much smaller than the wavelength. We consider three different shapes of the encapsulant top surface, namely a *flat* (no cap), a *convex* (spherical cap with height $h = r/2$) and a *hemispherical* (spherical cap with height $h = r$). 100 000 rays are traced in the simulations, which is sufficient for obtaining an ergodic distribution.

Figure 9(a) shows the simulated phosphorescence extraction efficiency, i.e. the phosphorescence power extracted into the free space divided by the phosphorescence power generated inside the package, for different types of packages. The package with remote phosphor, diffuse reflector cup and hemispherical encapsulant dome has the highest phosphorescence extraction efficiency (η_{ex}). The extraction efficiency is improved by up to 50% over that of proximate-phosphor-in-specular-cup configuration with flat encapsulant. For the flat and hemispherical encapsulant, η_{ex} is greatly improved by employing the remote phosphor concept. For the proximate phosphor distribution with a convex cap, the phosphor is closest to the centre point of the spherical cap, which results in a high extraction efficiency. The influence of the separation between the phosphor and the LED chip on extraction efficiency (η_{ex}) is simulated by varying the cup height. In the simulation, the remote phosphor layer is always on the top of reflector cup and the LED chip is placed at the cup's bottom centre, so that the increase of cup height also increases the distance between the LED chip and the

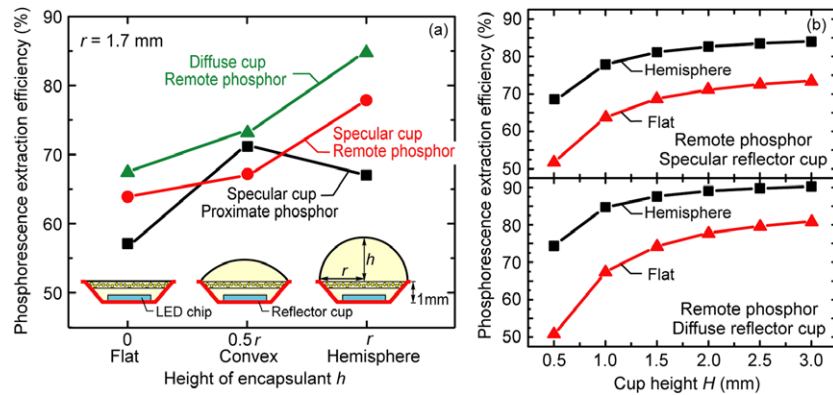


Figure 9. (a) Simulated phosphorescence-extraction efficiency for different types of packages. (b) The phosphorescence extraction efficiency increases with increasing cup height for both specular and diffuse reflector cups.

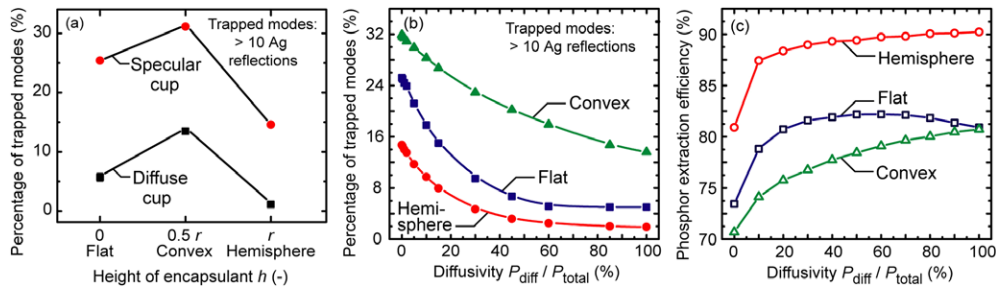


Figure 10. (a) Percentage of trapped modes (> 10 Ag reflections) inside the white LED lamps with remote phosphor for a flat, convex and hemispherical encapsulant shape. Influence of diffusivity of reflector cup on (b) percentage of trapped modes and (c) phosphor extraction efficiency.

phosphor layer. The simulation results, given in figure 9(b), clearly show that η_{ex} is improved by increasing the separation between the phosphor layer and the LED chip, confirming our predictions.

It is apparent from the simulations that the diffuse reflector cup enhances the extraction of phosphorescence. We believe that the enhancement is due to the reduction of whispering-gallery modes by the diffuse reflector cup which randomizes the propagation direction of trapped optical rays in the packages. The fraction of trapped modes for different encapsulation geometries and reflector cups are simulated, as shown in figure 10, to demonstrate the existence of whispering-gallery modes. We define trapped optical modes as modes that incur more than 10 reflection events from the Ag reflector cup. For a lamp package with specular reflector cup, 25%, 32% and 14% of the emission rays are trapped for a flat, convex and hemispherical encapsulation shape, respectively. By employing a diffuse reflector cup, the fraction of trapped modes is significantly reduced, irrespective of the encapsulant geometry. 58% and 86% of trapped modes are extracted out into free space by employing a diffuse reflector cup for convex and hemispherical encapsulation shapes, respectively.

Diffusivity is one of the most important parameters for a roughened reflector, which directly influences the extraction of whispering-gallery modes. According to our simulations, the fraction of trapped modes decreases rapidly with increasing reflector diffusivity, as shown

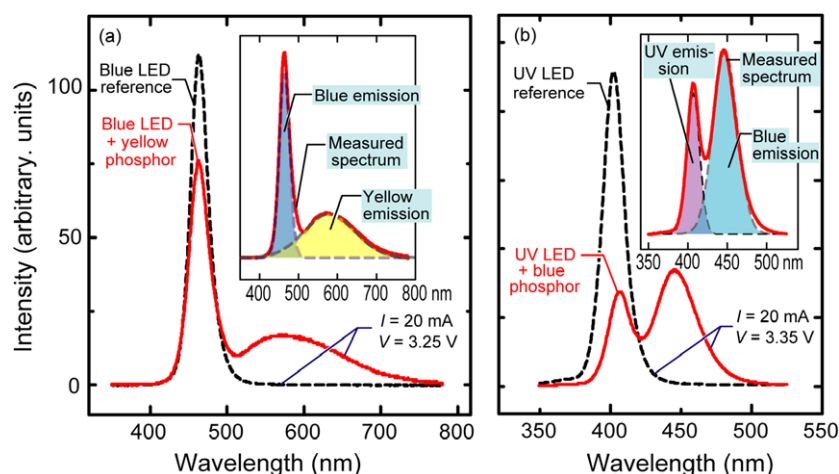


Figure 11. Emission spectra (—) of a blue-pumped white LED lamp with yellow phosphor and a UV-pumped dichromatic LED lamp with blue phosphor. The dashed lines show the emission from reference LEDs packaged without phosphor. De-convolution of the spectra into emission from the LED chip and emission from the phosphor is shown in the inset.

in figure 10(b). For a reflector cup with a diffusivity of 86%, the percentage of trapped modes decreases to 4.8%, 14.7% and 2.0% for flat, convex and hemispherical encapsulant shapes, respectively. Accordingly, the phosphorescence extraction efficiency η_{ex} is improved with increasing diffusivity of the reflector cup, as shown in figure 10(c). There is a slight decrease in efficiency for lamps with a flat encapsulant when the diffusivity of the cup exceeds 60% although the trapped modes are reduced. It is believed that the decrease in efficiency is caused by the Lambertian reflection pattern, which guides a small amount of the light down to the absorptive LED chip.

Two types of dichromatic LED lamps have been fabricated, one of them comprising a UV GaInN LED ($\lambda = 400$ nm) pumping a blue phosphor and the other one comprising a blue GaInN LED ($\lambda = 470$ nm) pumping a yellow phosphor. Different phosphor arrangements and reflector cups are employed. For diffuse reflector cups, the sidewalls are roughened by bead-blasting to achieve diffuse reflection. The LED chips are die-bonded to the bottom of the reflector cups followed by the wire bonding process. For the proximate phosphor configuration, the phosphor is uniformly mixed into an epoxy resin and filled into the reflector cup. For the remote phosphor configuration, the transparent epoxy resin (without phosphor) is filled into the reflector cup and cured. Then, a layer of phosphor and epoxy mixture is uniformly coated on the top of the cured epoxy, as shown in figure 5(c). After the phosphor and epoxy mixture layer is cured, reflector cups containing an LED chip and a phosphor are encapsulated by the standard LED packaging technology. LEDs without phosphor are packaged as *reference lamps* that are used to calculate the phosphor conversion efficiency.

The emission spectra of the reference LED emitters and of the dichromatic lamps operating at 20 mA, shown in figure 11, are measured using an integrating sphere. As illustrated in the inset, the spectra of dichromatic lamps were de-convoluted into primary LED emission and phosphorescence emission. By integrating the de-convoluted spectra, the optical power of each part is obtained. Table 3 shows the phosphor power conversion efficiencies, which are calculated by dividing the measured optical power from the phosphor by the difference in optical power between the LED emission of the reference lamp (without phosphor) and primary LED emission of the dichromatic lamp. For the dichromatic white lamp with the blue LED

Table 3. Phosphor power-conversion efficiency of dichromatic LED lamps with different reflector cup and phosphor configurations. The numbers in the parenthesis show the enhancement of phosphor power-conversion efficiency compared with that of a specular cup with proximate phosphor configuration. The power conversion efficiency given in the table is the product of the wavelength conversion efficiency, $\eta_w = (h\nu_1 - h\nu_2)/h\nu_1$, and the phosphor quantum efficiency.

	Phosphor power conversion efficiency (%)	
	UV LED + blue phosphor	Blue LED + yellow phosphor
Specular cup	67.9	59.9
Proximate phosphor	(-)	(-)
Specular cup	76.8	64.6
Remote phosphor	(13.1%)	(7.8%)
Diffuse cup	86.2	69.4
Remote phosphor	(27.0%)	(15.4%)

pumping the yellow phosphor, the phosphor conversion efficiency is improved by 7.8% for the remote phosphor with specular cup configuration and by 15.4% for the remote phosphor with diffuse cup configuration over the proximate-phosphor-in-specular-cup configuration. As for the UV-pumped blue phosphor configuration, the enhancement of power conversion efficiency is even higher due to the low reflectivity of the Ag reflector at short wavelengths. A 27% improvement is obtained for the remote phosphor with diffuse cup configuration compared with the proximate-phosphor-in-specular-cup configuration. These experimental results are fully consistent with the ray tracing simulations, confirming the enhancement of phosphor efficiency by employing a diffuse reflector cup with the remote phosphor configuration.

3. Omni-directional reflectors for light-emitting diodes

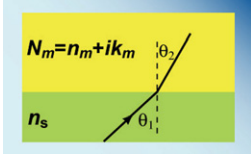
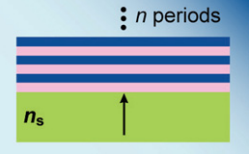
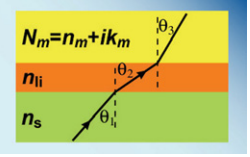
This section discusses possible solutions to limitations in light-extraction efficiency of light-emitting diodes (LEDs) using new types of triple-layer omni-directional reflectors (ODRs). The ODRs have lower mirror losses than metal reflectors and distributed Bragg reflectors (DBRs). High-reflectivity ODRs have been incorporated into GaInN LEDs and AlGaInP LEDs. It is shown that the ODR significantly increases light extraction from ODR-LEDs as compared to reference LEDs employing a DBR or a metal reflector.

3.1. Reflectors for light-emitting diodes

One of the fundamental ways to reduce optical losses in light-emitting devices is the employment of optical reflectors with *near-perfect reflection characteristics*. For example, a strong optical loss mechanism in GaInN-based flip-chip LED structures is due to the low reflectivity of the p-type contact such as oxidized Ni/Au. Because multiple reflection events can occur in LED structures, mirror losses should be kept at a minimum by using reflectors with near-perfect reflection characteristics. Such near-perfect characteristics of a reflector include (i) high reflectivity, (ii) omni-directionality, (iii) broad spectral range of the high-reflectivity band and (iv) electrical conductivity for current-injected structures.

There are several reflectors used in current LED structures including metal reflectors, DBRs and ODRs. The structure and the optical/electrical characteristics of these reflectors are given in table 4. *Metal reflectors* are electrically-conducting reflectors capable of

Table 4. Schematic structures and electrical/optical characteristics of metal reflectors, distributed Bragg reflectors (DBRs) and triple-layer omni-directional reflectors (ODRs).

	Metal reflector	Distributed Bragg reflector (DBR)	Triple-layer omni-directional reflector (ODR)
Structure			
Reflectivity ^a	<95%	~99%	~99%
Omni-directionality	Yes	No	Yes
Spectral width	Broad	Narrow	Broad
Electrical conductivity	Good	—	—

^a Reflectivity depends on wavelength and optical properties of reflector materials.

reflecting visible light over a wide range of wavelengths and incident angles, i.e. showing omni-directionality and broad spectral width. However, reflectivity of metal reflectors on semiconductors is typically at most 95%. For example, Ag, which shows highest reflectivity among metals at visible wavelengths, exhibits normal-incidence reflectivity on GaN of ~91% at 470 nm. DBRs are periodic structures with a unit cell of two dielectric layers having different refractive indices n_i and quarter-wavelength thicknesses d_i ($i = 1, 2$). DBRs can be considered as one-dimensional photonic crystals that have a high-reflectivity stop band due to the non-propagating light states in the structure. Therefore, one can design a DBR to have a reflectivity as high as ~99% at a certain centre wavelength for normal incidence. However, the DBR reflectivity depends on the incidence angle θ so that the stop band shifts towards shorter wavelengths for increasing θ without changing its spectral width. As a result, DBRs become transparent for oblique angles of incidence. In addition, the reflectivity of DBRs also depends on the polarization of the incident light. According to Brewster's law, the reflection of light polarized parallel to the plane of incidence (TM mode) has a minimum at the Brewster angle $\theta_B = \arctan(n_1/n_2)$, where n_1 and n_2 are the refractive indices of the two adjoining media. Therefore, the overall reflectivity, (TM mode + TE mode)/2, significantly decreases near θ_B . Furthermore, the applicability of DBRs in LEDs is limited due to the electrically insulating and thermally-resistant nature of dielectric layers.

Recently, a very promising *triple-layer ODR* suitable for LED technology has been introduced. The triple-layer ODR comprises a semiconductor with a refractive index n_s , a low-refractive index layer (n_{li}) and a metal with a complex refractive index $N_m = n_m + ik_m$, where k_m is the extinction coefficient. Triple-layer ODRs with high reflectivity, wide stop band and omni-directional reflection characteristics have been demonstrated and have shown the ability to easily outperform metal reflectors and DBRs [24–26].

The reflectance of a semiconductor/metal reflector as a function of the incident angle θ is given by [27]

$$R_{TE} = \left| \frac{n_s \cos \theta_1 - N_m \cos \theta_2}{n_s \cos \theta_1 + N_m \cos \theta_2} \right|^2 \quad \text{and} \quad R_{TM} = \left| \frac{\frac{n_s}{\cos \theta_1} - \frac{N_m}{\cos \theta_2}}{\frac{n_s}{\cos \theta_1} + \frac{N_m}{\cos \theta_2}} \right|^2. \quad (7)$$

The reflectance of the triple-layer ODR as a function of the incident angle θ is given by [27]

$$R = \left| \frac{r_{01} + r_{12} \exp(2i\phi)}{1 + r_{01}r_{12} \exp(2i\phi)} \right|^2, \quad (8)$$

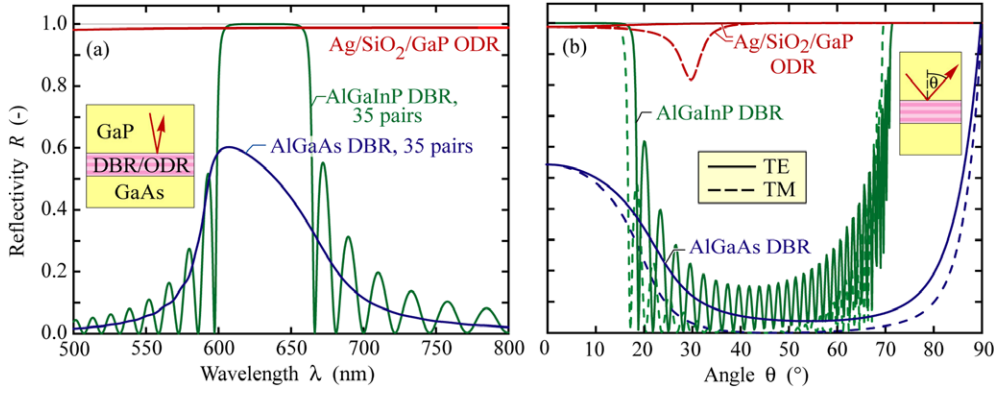


Figure 12. Calculated reflectivity for a 35-period $(\text{Al}_{0.3}\text{Ga}_{0.7})_{0.5}\text{In}_{0.5}\text{P}/\text{Al}_{0.5}\text{In}_{0.5}\text{P}$ DBR, a 35 period AlAs/GaAs DBR and a triple layer ODR (GaP/SiO₂/Ag). GaP was chosen as the external medium. (a) Reflectivity versus wavelength for normal incidence and (b) angular dependence of the reflectivity at 630 nm (after Gessmann and Schubert [25]).

where

$$r_{01\text{TE}} = \frac{n_s \cos \theta_1 - n_{li} \cos \theta_2}{n_s \cos \theta_1 + n_{li} \cos \theta_2}, \quad r_{01\text{TM}} = \frac{n_{li} \cos \theta_1 - n_s \cos \theta_2}{n_{li} \cos \theta_1 + n_s \cos \theta_2},$$

$$r_{12\text{TE}} = \frac{n_{li} \cos \theta_2 - N_m \cos \theta_3}{n_{li} \cos \theta_2 + N_m \cos \theta_3}, \quad r_{12\text{TM}} = \frac{N_m \cos \theta_2 - n_{li} \cos \theta_3}{N_m \cos \theta_2 + n_{li} \cos \theta_3}$$

and
$$\phi = \frac{2\pi}{\lambda} n_{li} h \cos \theta_2.$$

Equation (8) applies to a low-index dielectric layer thickness of $\lambda_0/(4n_{li})$, i.e. to a quarter wavelength layer. Figure 12 shows calculated reflectivity for an Ag/SiO₂/GaP ODR and two DBRs, an AlGaInP DBR and an AlGaAs DBR, both incorporated in an AlGaInP LED emitting at 630 nm. The AlGaAs DBR consists of 35 periods of AlAs/GaAs and the AlGaInP DBR consists of 35 periods of $(\text{Al}_{0.3}\text{Ga}_{0.7})_{0.5}\text{In}_{0.5}\text{P}/\text{Al}_{0.5}\text{In}_{0.5}\text{P}$, designed to have a high normal-incidence reflectivity at the centre wavelength of 630 nm, as shown in figure 12(a). The AlGaInP DBR shows a narrow high-reflectivity stop band between 600 and 670 nm, while the reflectivity of Ag/SiO₂/GaP ODR shows high reflectivity for all visible wavelengths. Figure 12(b) compares the angular dependence of reflectivity of an Ag/SiO₂/GaP ODR with the two DBRs. While the ODRs maintain high reflectivity at virtually all angles of incidence, the AlGaInP DBR reflectivity sharply drops above 17°. Note that the reflectivity of the triple-layer ODR is significantly better at oblique angles of incidence than that of DBRs. It was also shown that the angular-averaged reflectivity of the Ag/SiO₂/GaP ODR is much higher than that of a 20 period $\text{Al}_{0.25}\text{Ga}_{0.75}\text{N}/\text{GaN}$ DBR and Ag metal reflector at 470 nm ($n_{\text{Ag}} = 0.132$, $k_{\text{Ag}} = 2.72$, $n_{\text{SiO}_2} = 1.46$, $n_{\text{GaN}} = 2.454$ at 470 nm) [25]. High reflectivity is essential to minimize the losses of waveguided modes which are common in LEDs. These theoretical considerations show the huge advantages offered by ODRs.

3.2. GaInN blue light-emitting diodes with omni-directional reflectors

Recently, GaN blue LEDs having new types of ODRs with high reflectivity, wide stop band and omni-directional reflection characteristics have been demonstrated [26, 28, 29]. Figure 13(a) shows a typical GaN-based LED structure comprising a mesa with the common ‘p-side-up’

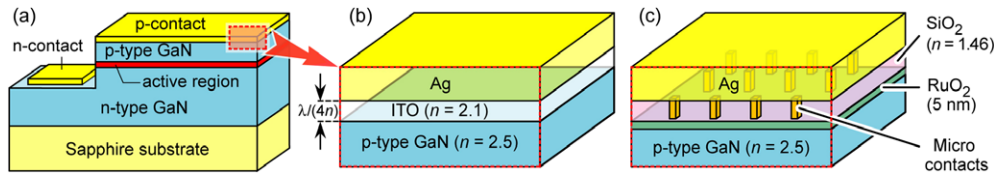


Figure 13. (a) Typical GaInN-based LED structure comprising a mesa with common ‘p-side-up’ growth on sapphire substrate. Schematic cross-sectional view of (b) a GaN/ITO/Ag ODR (after Gessmann *et al* [29]) and (c) a GaN/RuO₂/SiO₂/Ag ODR. The SiO₂ low-refractive-index layer is perforated by micro-contacts enabling electrical conductivity between the RuO₂ contact layer and Ag (after Kim *et al* [26]).

growth on a sapphire substrate. The first ODR structure incorporated into a GaN blue LED is shown in figure 13(b) [29]. The ODR consists of GaN, a transparent and electrically conductive ITO with quarter-wavelength thickness and a Ag layer, based on high/low/high complex refractive index of the Ag ($n_{\text{Ag}} = 0.132$, $k_{\text{Ag}} = 2.72$ at 470 nm), ITO ($n_{\text{ITO}} = 2.06$ at 470 nm) and GaN ($n_{\text{GaN}} = 2.45$ at 470 nm). The GaN LED structure was grown by organometallic vapour-phase epitaxy (OMVPE) and consists of a thick n-type GaN buffer layer, an n-type GaN lower cladding layer, a GaInN/GaN multiple quantum well active region, a p-type GaN upper cladding and a highly doped contact layer. LED mesa structures were fabricated by standard photolithographic patterning followed by dry-etching to expose the n-type cladding layer. After a 3 min dip in buffered oxide etchant (BOE), p-type contacts for the ODR-LEDs were deposited in a two-step process: first, an ITO film of quarter wavelength thickness was deposited by RF-assisted sputtering. The ITO was then annealed in a rapid thermal annealing (RTA) furnace at 600 °C under an N₂ atmosphere for 30 s. The ITO film was virtually colourless and transparent. In the second step, Ag (200 nm) and Au (20 nm) were deposited on top of the annealed ITO layer by electron-beam evaporation. For comparison, LEDs with conventional Ni/Au contacts were fabricated on the same wafer. The n-type contacts for both samples were fabricated by electron-beam evaporation of Ti/Al (60/60 nm) contacts without oxide removal or subsequent annealing. It was shown that the ODR-LEDs have lower optical losses and higher extraction efficiency as compared with conventional LEDs with Ni/Au contacts. However, the ODR-LED showed a high forward voltage, possibly due to a high contact resistivity of ITO/p-GaN.

An ODR structure that includes a RuO₂ current-spreading layer has been incorporated into a GaInN blue LED as shown in figure 13(c) [26]. The ODR comprises GaN, a thin layer of oxidized ruthenium (Ru) used as semitransparent low-resistance p-type ohmic contact a quarter-wave thick SiO₂ low-refractive index layer perforated by an array of Ag micro-contacts, and a thick Ag layer. The GaInN LED structure was grown by OMVPE on c-plane sapphire substrate. After a dry-etching for LED mesa structure, Ru (5.0 nm) was deposited on p-type GaN and annealed at 500 °C in an O₂ atmosphere to form RuO₂ which acts as an ohmic contact to p-type GaN. The RuO₂ obtained by this oxidation annealing was virtually colourless and transparent. A quarter-wave thick SiO₂ layer was deposited on the RuO₂ using plasma-enhanced chemical vapour deposition (PECVD). Then, an array of circular micro-contacts was etched into the SiO₂, by using BOE, to expose the conducting RuO₂ layer. Ag (200 nm) and Au (20 nm) were deposited by electron-beam evaporation on top of the SiO₂ patterned with micro-contact holes. For comparison, LEDs with conventional Ni/Au and Ag contacts were fabricated on the same wafer. The n-type contacts formed readily by electron-beam deposition of Ti/Al/Ni/Au (30/120/40/50 nm). No oxide removal or subsequent annealing was needed for contact formation.

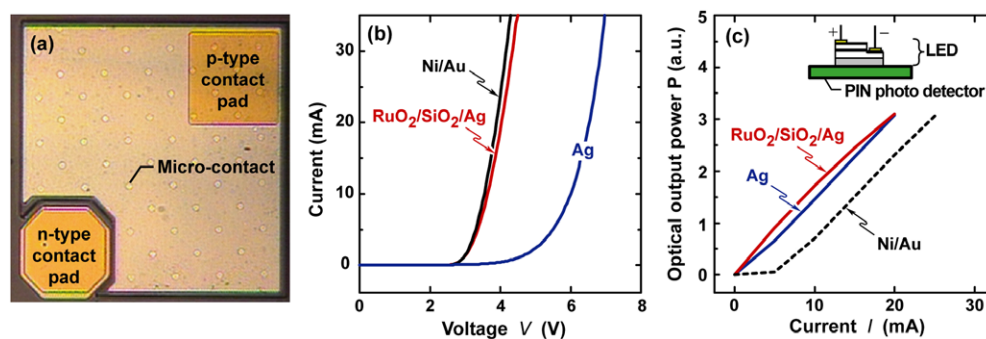


Figure 14. (a) Top view of the GaInN LED with GaN/RuO₂/SiO₂/Ag ODR. The SiO₂ lowrefractive-index layer is perforated by micro-contacts enabling electrical conductivity between the RuO₂ contact layer and Ag. (b) Current–voltage characteristics and (c) light-output-versus-current characteristic of GaInN LED with GaN/RuO₂/SiO₂/Ag ODRs and LEDs with Ni/Au and Ag contacts (after Kim *et al* [26]).

Figure 14(a) shows a top view of the GaInN LED with GaN/RuO₂/SiO₂/Ag ODR. The chip dimensions are $300 \times 300 \mu\text{m}^2$. There is an array of circular micro-contacts in the p-contact area, enabling electrical conductivity between the RuO₂ contact layer and Ag through the insulating SiO₂ low-index layer. The diameter of the micro-contacts is $4 \mu\text{m}$. Figure 14(b) shows I – V characteristics of the LED with GaN/RuO₂/SiO₂/Ag ODR and the conventional LEDs with Ni/Au and Ag contacts. The forward voltage at 20 mA for the LED with GaN/RuO₂/SiO₂/Ag ODR is 4.0 V, comparable to that of the conventional LED with Ni/Au contact, 3.9 V. This indicates that the contact resistivity of RuO₂ on p-type GaN is comparable to that of Ni/Au. Because the RuO₂ contact layer, one of the conducting metal oxides, has a low resistivity ($\sim 50 \mu\Omega \text{cm}$) and a high work function ($> 5 \text{eV}$), the material acts as an excellent current spreading and low-resistance contact layer to p-type GaN. On the other hand, the forward voltage of the LED with a Ag contact is as high as 6.5 V. This is due to a low work function of Ag (4.26 eV), resulting in a high potential barrier between Ag and p-type GaN.

The electroluminescence intensity from the backsides of the LEDs was measured directly on a large-size ($10 \times 10 \text{mm}^2$) Si PIN photodetector. The light-output-versus-current characteristic of the LEDs is shown in figure 14(c). At small forward currents ($I < 20 \text{mA}$), the light power extracted from the LED with ODR is slightly larger than the output from the LED with an Ag contact, but significantly larger than that from the LED with a Ni/Au contact. The increased light output of the LED with ODR can be attributed to a higher reflectivity and hence better light-extraction efficiency due to the use of the ODR. In addition, saturation of the light output power with increasing current level is not observed for the LED with GaN/RuO₂/SiO₂/Ag ODR, indicating that the resistivity of the RuO₂ layer and specific contact resistance of the GaN/RuO₂ contact is sufficiently low for LED applications.

Oblique-angle deposition is a method to grow highly porous thin films consisting of an array of nano-rods. The nano-rod growth is caused by the self-shadowing nature of the oblique-angle deposition process. This process will be described in detail in the next section. Several nano-rod ITO films, grown by oblique-angle electron-beam deposition on Si substrates with a vapour flux incident angle θ of 80° , are found to be optically transparent and electrically conductive. Pure ITO granules are used as evaporation source, and the deposition rate is well controlled at 0.5nm s^{-1} . Figure 15(a) shows the cross-sectional scanning electron micrograph (SEM) of the nano-rod ITO layer. The nano-rod ITO is uniformly distributed with a tilt angle

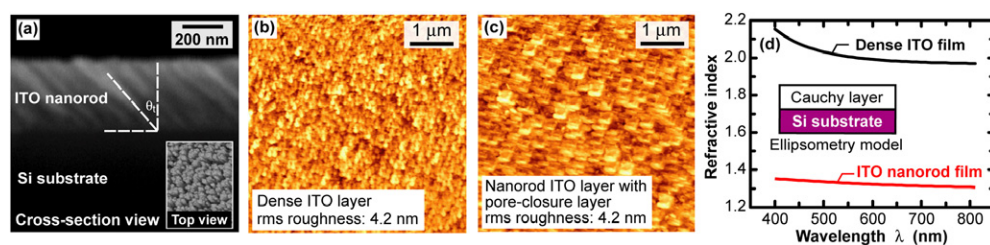


Figure 15. (a) Cross-sectional scanning electron micrograph (SEM) of the ITO nano-rod layer on Si substrate. Inset shows the top view of the ITO nano-rod layer. Atomic force micrographs of the surface of (b) dense ITO layer and (c) ITO nano-rod layer with pore-closure ITO layer. (d) Refractive index of dense ITO and low- n ITO films versus wavelength measured using ellipsometry.

of $\theta_i = 45^\circ$. The gap between the nano-rod ITO is less than 50 nm, i.e. much smaller than the wavelength of visible light, thereby limiting optical scattering. The nano-rod ITO thin film obtained by the oblique-angle deposition is specular, featureless and virtually colourless and transparent. Furthermore, since the film is deposited by evaporation, the controllability of film thickness is excellent, very suitable for quarter-wavelength thickness optical films. Therefore, oblique-angle deposition is promising for the growth of optical coatings with very low-refractive index, which are advantageous for ODRs with high-refractive-index contrast. The inset in figure 15(a) shows the SEM top view of the nano-rod ITO film including openings between the nano-rods. In order to avoid the filling of subsequent metal into these openings, a surface-sealing step is employed by depositing an ITO pore-closure layer. The atomic-force micrographs (AFM) of the surface of the dense ITO layer and the nano-rod ITO layer with pore-closure layer are shown in figures 15(b) and (c), respectively. The root-mean-square (rms) surface roughness of the dense ITO layer, which is electron-beam deposited with normal incidence of the vapour flux, is 4.2 nm. The rms roughness of the nano-rod ITO layer without pore-closure layer is 8.3 nm, higher than that of the dense ITO layer, due to the openings between the nano-rods. After the pore-closure layer deposition, the rms roughness reduces to 4.2 nm, and there is no indication of openings between the nano-rods, as shown in figure 15(c).

The refractive index of the nano-rod ITO films is measured with ellipsometry using the incident angles 60° , 65° and 70° . A 'Cauchy layer on Si substrate' is used as the ellipsometry model and found to fit the measurement data very well. The refractive index of the nano-rod ITO films versus wavelength is shown in figure 15(d). Over the entire visible spectrum, the refractive index of the nano-rod ITO layer is $n < 1.35$. At 461 nm, the refractive index of the nano-rod ITO layer is $n = 1.34$, much lower than the refractive index of dense ITO, $n = 2.06$, and even lower than that of SiO_2 , $n = 1.46$.

The low- n ITO is incorporated into a GaInN LED emitting at a peak wavelength of 474 nm. The GaInN LED structure was grown by OMVPE on c-plane sapphire substrate and consists of a $3 \mu\text{m}$ thick n-type GaN buffer layer, an n-type GaN lower cladding layer, a GaInN/GaN multiple quantum well active region, a p-type GaN upper cladding and a highly doped p-type GaN contact layer. A quarter-wavelength-thick low- n ITO layer was deposited by oblique-angle electron-beam deposition with an incident angle of 80° . After the low- n ITO deposition, a very thin (20 nm) pore-closure layer is formed on top of the low- n ITO layer with an incident angle of -45° . After the pore-closure layer, a 200 nm-thick Ag layer is deposited by electron-beam evaporation. LED mesa structures were obtained by standard photolithographic patterning followed by chemically-assisted ion-beam etching using Cl_2 and Ar to expose the n-type cladding layer. For comparison, LEDs with an Ag reflector were fabricated on the same wafer piece.

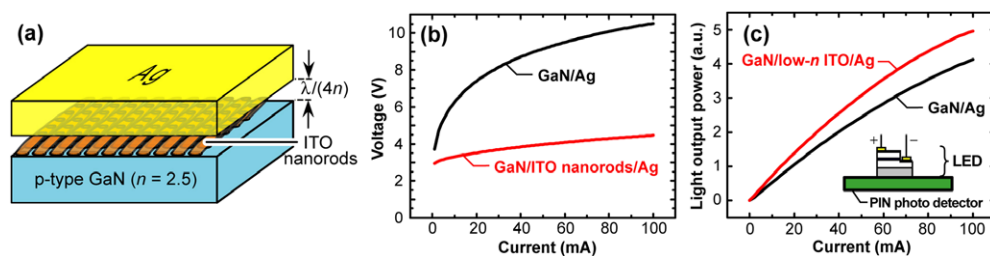


Figure 16. (a) GaInN LED with GaN/low-*n* ITO/Ag ODR. (b) Current–voltage characteristics and (c) light-output-versus-current characteristics of a typical GaInN LED with GaN/low-*n* ITO/Ag ODR and of a typical LED with Ag reflector.

Figure 16(a) schematically shows the GaInN LED having an ODR with the low-*n* ITO layer. The n-type contact for all samples is electron-beam evaporated Ti/Al/Ni/Au annealed at 650°C for 1 min. Figure 16(b) shows typical current–voltage characteristics of the LEDs with GaN/low-*n* ITO/Ag ODR and of the LEDs with Ag reflector. The forward voltage at 20 mA for the GaN/low-*n* ITO/Ag ODR LEDs is 3.5 V, much lower than that for the LEDs with Ag reflector. The electroluminescence intensity from the backside of the LED was measured directly on a large-size (10 × 10 mm²) Si PIN photodetector. A typical light-output-versus-current characteristic of the LEDs is shown in figure 16(c). The light-output power of the GaN/low-*n* ITO/Ag ODR LEDs is significantly higher than that of the LEDs with the Ag reflector. At an injection current of 20 mA, the enhancement in light-output of the LEDs with GaN/low-*n* ITO/Ag ODR is 31.6% compared with the LEDs with the Ag reflector. The increased light-output of the LEDs with GaN/low-*n* ITO/Ag ODR is attributed to higher reflectivity and lower loss of waveguided optical modes. The better light-extraction efficiency is due to the high refractive-index contrast enabled by the low-*n* ITO layer.

3.3. GaInN near ultraviolet light-emitting diodes with omni-directional reflectors

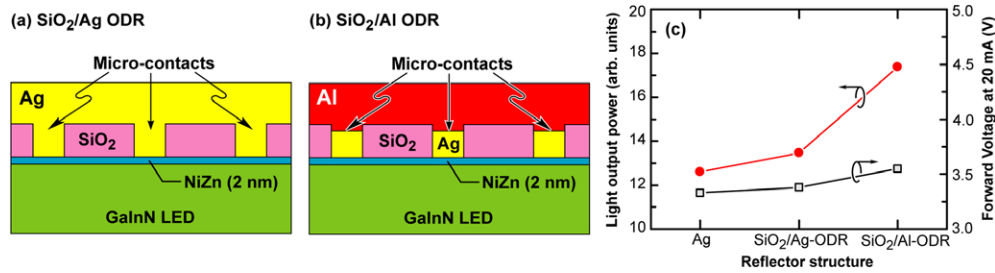
Short-wavelength light sources such as GaInN-based near-ultraviolet (UV) and blue LEDs can be used as efficient excitation sources for organic and inorganic luminescent materials for down-converting photon energies. For example, a near UV GaInN LED chip pumping red, green and blue phosphors results in tri-chromatic white light with excellent colour-rendering index by means of mixing the three complementary colours. Therefore, it is important to develop reflectors with high reflectivity for LEDs emitting near UV wavelengths of ~400 nm for general illumination applications.

Ag-based reflectors have been widely used for GaN LEDs emitting in the green and blue because Ag shows high reflectivity at *visible* wavelengths and good ohmic properties with p-type GaN when used with an adhesion-promotion layer such as NiZn [30]. However, the reflectivity of Ag decreases rapidly as the emission wavelength approaches near-UV range due to a rapid decrease in the Ag extinction coefficient and increase in the Ag index of refraction. Al-based reflectors can be a good alternative because of the relatively high extinction coefficient and low index of refraction of Al in the UV wavelength range. However, Al shows poor ohmic contact properties to p-type GaN.

The normal-incidence reflectivity, $R(\theta) = (R_{TE} + R_{TM})/2$, of two ODRs (GaN/SiO₂/Ag and GaN/SiO₂/Al) and an Ag reflector at $\lambda = 470$ and 400 nm, is given in table 5. The reflectivity values are calculated using parameters: $n_{\text{GaN}} = 2.5$, $n_{\text{SiO}_2} = 1.47$, $n_{\text{Ag}} = 0.173$, $k_{\text{Ag}} = 1.95$, $n_{\text{Al}} = 0.49$, $k_{\text{Al}} = 4.86$ for $\lambda = 400$ nm and $n_{\text{GaN}} = 2.4$, $n_{\text{SiO}_2} = 1.46$,

Table 5. Normal-incidence reflectivity $R(\theta) = (R_{TE} + R_{TM})/2$ of two ODRs (GaN/SiO₂/Ag and GaN/SiO₂/Al) and a Ag reflector on GaN at $\lambda = 400$ and 470 nm.

	Ag	SiO ₂ /Ag ODR	SiO ₂ /Al ODR
Normal-incidence reflectivity ($\lambda = 470$ nm)	0.906	0.942	0.929
Normal-incidence reflectivity ($\lambda = 400$ nm)	0.842	0.877	0.933

**Figure 17.** Schematic cross-sectional view of GaInN LED with (a) GaN/SiO₂/Ag ODR and (b) GaN/SiO₂/Al ODR. (c) Light output and forward voltage at 20 mA of the LEDs for different reflector structures: Ag reflector, GaN/SiO₂/Ag ODR and GaN/SiO₂/Al ODR.

$n_{\text{Ag}} = 0.135$, $k_{\text{Ag}} = 2.7$, $n_{\text{Al}} = 0.68$, $k_{\text{Al}} = 5.6$ for $\lambda = 470$ nm. The table clearly shows that the normal-incidence reflectivity is enhanced for the GaN/SiO₂/Al ODR compared with both the GaN/SiO₂/Ag ODR and the Ag reflector. In addition to the normal-incidence results, the angle-dependent reflectivity is also enhanced for the GaN/SiO₂/Al ODR compared with the GaN/SiO₂/Ag ODR and the Ag reflector. This is attributed to the higher reflectivity of triple-layer ODRs compared with metal reflectors and due to the higher extinction coefficient of Al ($k_{\text{Al}} = 4.86$) than that of Ag ($k_{\text{Ag}} = 1.95$) at $\lambda = 400$ nm.

GaN LEDs emitting at $\lambda = 400$ nm with GaN/SiO₂/Al ODR, GaN/SiO₂/Ag ODR and Ag reflector were fabricated in order to experimentally demonstrate the viability of Al-based ODRs. LED mesa structures were obtained by standard photolithographic patterning followed by chemically-assisted ion beam etching using Cl₂ and Ar to expose the n-type cladding layer. A thin NiZn (10 wt% of Zn) was deposited on p-type GaN by electron-beam evaporation followed by the deposition of quarter-wavelength-thick SiO₂ using PECVD. Then, an array of micro-contacts was patterned on SiO₂ and etched using BOE to expose the p-type GaN layer. Because of the poor ohmic property of Al on p-type GaN, Ag (60 nm) is deposited on micro-contact holes by electron-beam evaporation and lift off in a self-aligned process, followed by annealing in O₂ atmosphere to form a low-resistance ohmic contact. Then, the Al layer was deposited by electron-beam evaporation on the entire p-type GaN area. For comparison, LEDs with NiZn/Ag (2/60 nm) contacts and LEDs with GaN/SiO₂/Ag ODR were fabricated on different pieces of the same wafer. The n-type contacts for the samples were fabricated by electron-beam evaporation of Ti/Al/Ni/Au. Figures 17(a) and (b) show schematic cross-sectional views of a GaInN LED with GaN/SiO₂/Ag ODR, and with GaN/SiO₂/Al ODR, respectively.

Figure 17(c) shows light output and forward voltage at 20 mA of the LEDs with an Ag reflector, a GaN/SiO₂/Ag ODR and a GaN/SiO₂/Al ODR. The forward voltage at 20 mA for the GaN/SiO₂/Ag ODR LEDs is 3.37 V, almost the same as that for the LEDs with NiZn/Ag reflector, 3.32 V. This is attributed to the fact that the oxidized NiZn layer could

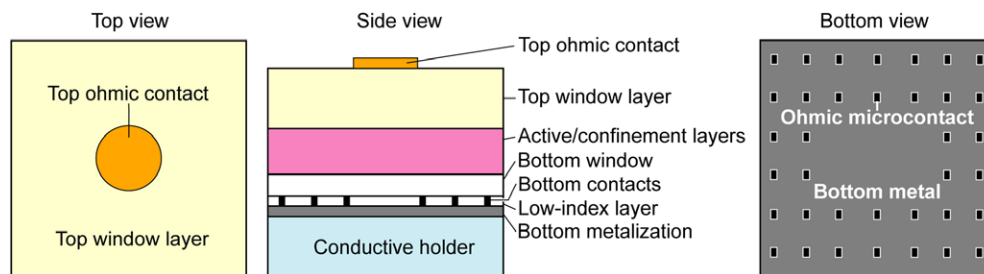


Figure 18. Top, cross-sectional and bottom views of AlGaInP LED incorporating a conductive ODR. The original GaAs substrate has been removed and the LED is bonded ‘p-side down’ to a conductive holder. The ODR also serves as p-type contact to the LED.

be a current-spreading and contact layer to p-type GaN with low contact resistivity. However, the forward voltage of the GaN/SiO₂/Al ODR LEDs is slightly higher, 3.55 V, than that of other devices. The electroluminescence intensity was measured directly from the backside of the LED by placing it on a large-size (10 × 10 mm²) Si PIN photodetector. At an injection current of 20 mA, the GaN near-UV LEDs with GaN/SiO₂/Al ODR show 16% and 38% higher light outputs than LEDs with SiO₂/Ag ODR and Ag reflector, respectively. The increased light-output of the LEDs with GaN/SiO₂/Ag and GaN/SiO₂/Al ODRs compared with LEDs with NiZn/Ag reflector is attributed to enhanced reflectivity of the ODR structures. In addition, the higher light-output of the LEDs with GaN/SiO₂/Al ODR compared with the LEDs with GaN/SiO₂/Ag ODR is attributed to enhanced reflectivity of the Al-based ODR at near-UV wavelengths, as expected from the theoretical calculation shown in table 5. It is worth discussing possible reasons why a ~10% enhancement of normal-incidence reflectivity leads to an enhancement of LED light output as high as 38%: multiple reflection events of trapped light occurring within the high-refractive-index semiconductor are a possible reason. If the bottom reflector has the reflectivity R , the light intensity after N reflection events is given by R^N . Calculation of R^N for $R < 1$ and $N \gg 1$ shows that a small difference in reflectivity can make a very large difference in light output.

3.4. AlGaInP light-emitting diodes with omni-directional reflectors

Figure 18 shows top, cross-sectional and bottom views of the AlGaInP LED with a conductive ODR. The AlGaInP LED consists of a top current-spreading layer (or window layer), the active and confinement layers, a bottom current-spreading layer (or window layer), the ODR, and a conductive holder such as a Si wafer. The active layers include the lower and upper confinement layers and the double heterostructure or multiple-quantum well active region. The wafer is grown in the standard ‘p-side up’ mode that is commonly employed for LEDs. The fabrication process includes deposition of the ODR, bonding of the wafer to a conductive holder such as Si, chemo-mechanical polishing for removal of the GaAs substrate and metal contact deposition on the top window layer.

Figure 19(a) shows a top-view of AlGaInP LEDs with ODR under current injection of 20 mA. The current–voltage characteristics of AlGaInP LEDs are shown in figure 19(b). A commercial AlGaInP absorbing-substrate (AS) LED emitting at 630–650 nm and a transparent-substrate (TS) LED emitting at 595 nm are used as references [31]. At a current of 20 mA, the forward voltage of the ODR-LED is about 2.7 V. Optical output power P versus injection current I for an ODR-LED, an AS-LED with a DBR and a TS-LED is shown in figure 19(c).

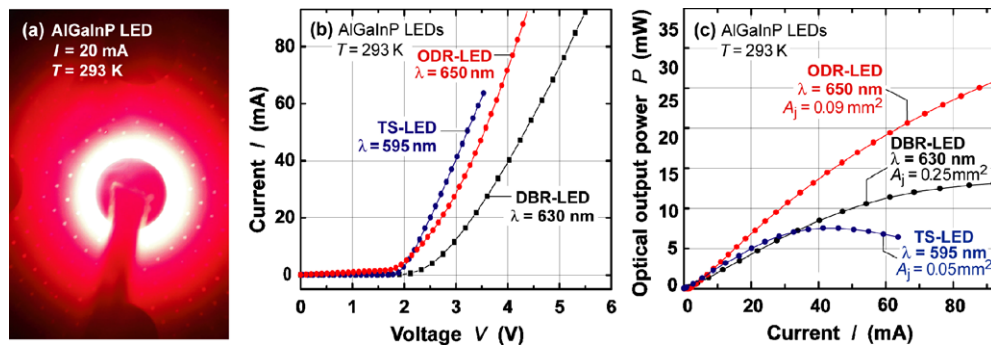


Figure 19. (a) Top-view micrograph of AlGaInP LED with ODR under current injection of 20 mA. (b) Current-versus-voltage characteristics and (c) dependence of the total optical output power on drive current for ODR-, DBR- and TS-AlGaInP LEDs emitting at 650 nm, 630 nm and 595 nm, respectively.

The peak wavelengths of the three devices are 650 nm (ODR-LED), 630 nm (DBR-LED) and 595 nm (TS-LED) with junction areas $A_j \approx 0.09$ mm², 0.25 mm² and 0.05 mm², respectively. In order to measure the total optical output power the samples were placed on a reflecting holder inside an integrating sphere. The largest light output is attained by the ODR-LED. Maximum values of the external quantum efficiencies η_{ext} are about 18% for the ODR-LED ($I_f = 27$ mA) and 11% for the DBR-LED ($I_f = 11$ mA). TS-LEDs operating at 632 nm have an external quantum efficiency of 32% [32]. The external quantum efficiency of the ODR device is expected to further increase with a thicker top window layer. The window layer thickness of the ODR device shown in figure 19 is 2 μ m and it is reasonable to expect an improvement by a factor of 2 for ODR devices with a thicker window layer.

4. Low-refractive-index optical thin films and their applications

4.1. Low-refractive-index materials

In distributed Bragg reflectors [33], the refractive index contrast, which is the difference in refractive index between the two constituting materials, is directly related to the reflectivity, spectral width of stop band and penetration depth. In optical micro-resonators [34], the effective cavity length and hence the enhancement of spontaneous emission directly depend on the index contrast. In photonic crystals [35], the photonic bandgap width is directly related to the index contrast. This motivates the development of novel optical materials with a refractive index much lower than that of any conventional thin-film material. We refer to this new class of materials as ‘low-refractive-index materials’ or ‘low- n materials’.

In semiconductor optoelectronics, the optical ambient material of a reflector frequently is a semiconductor, which is a high-refractive-index material with typical refractive index of 2.5–3.5. Note that optical reflection characteristics in this case are quite different from the case where air ($n = 1.0$) is the optical ambient material. Furthermore, optical reflectors for semiconductor optoelectronic devices require materials with a very low refractive index. For example, in the omni-directional reflector designs for semiconductor optoelectronic devices, the low- n material is a key part as demonstrated by Xi *et al* [36, 37].

Although multilayer structures with air-gaps have been demonstrated [33], the fabrication process requires under-etching and hence is slow and costly. Moreover, air gaps completely

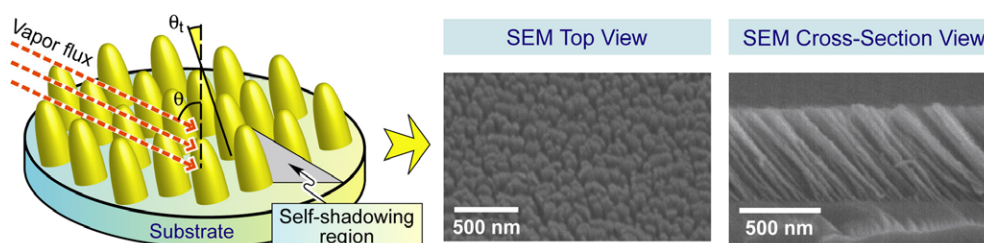


Figure 20. Mechanism of porous thin-film growth using oblique-angle deposition and scanning-electron micrographs of SiO₂ nano-rod thin film.

lack structural stability, making them unsuitable for most applications. MgF₂, CaF₂ and SiO₂ are materials with refractive indices among the lowest available for conventional, dense optical coatings. However, their refractive indices, $n_{\text{MgF}_2} = 1.39$, $n_{\text{CaF}_2} = 1.44$, $n_{\text{SiO}_2} = 1.46$, are much higher than the refractive index of air, 1.0. Nano-porous dielectric materials have a lower refractive index than dense materials and such nano-porous materials are a promising direction for the development of low- n materials. We point out that the low- n materials discussed here have distinctly different requirements than the low- k materials used in Si microelectronics technology. In contrast to low- k materials, low- n materials require that Mie and Rayleigh scattering, which is irrelevant to low- k materials, be minimized.

Several low- n materials are currently being developed. Nano-porous SiO₂ thin films fabricated from a sol-gel process [38–40] have a very low refractive index, good mechanical strength and low scattering coefficients. Its refractive index can be as low as 1.10 [37, 39]. Nano-porous SiO₂ fabricated from a sol-gel process has an average pore size 4 nm [41]. Optical scattering from such nano-structure pores is indeed expected to be very small. However, it may be difficult to precisely control the thickness and the uniformity of spin-on sol-gel materials.

Teflon AF has a refractive index of 1.32 and is transparent in the visible spectrum. Teflon AF has the lowest refractive index among available organic polymer materials. However, its refractive index is not sufficiently low and, since it requires a spin coating process for deposition, its film thickness may be difficult to control. Thus, to obtain viable low- n materials, new materials and fabrication methods are needed.

4.2. Oblique-angle deposition for films consisting of an array of nano-rods

Oblique-angle deposition was introduced in the 1950s [42]. It is a technology to grow porous, sculptured thin films [43, 44] enabled by the self-shadowing effect and surface-diffusion effect [45] during the deposition process [46, 47]. Since the films resulting from oblique-angle deposition can have very high porosity, it can be used to fabricate low- n thin film materials. Figure 20 shows the deposition mechanism of oblique-angle deposition. A random growth fluctuation on the substrate produces a shadow region that the subsequent incident vapour flux cannot reach. Also produced are ‘hills’ where the incident flux deposits preferentially, thereby creating an array of oriented rods with tilt angle of θ_t . In oblique-angle deposition, the pore size of the porous thin film is determined, among other factors, by random growth fluctuations. This results in average pore sizes, i.e. separations between nano-rods, which are very small. In order to grow highly porous thin films, the incidence angle of the vapour flux with respect to the substrate normal, θ , must be large, preferentially close to 90° (grazing angle) [44]. To have a uniform and random distribution of nano-rods, the substrate’s initial surface should be smooth.

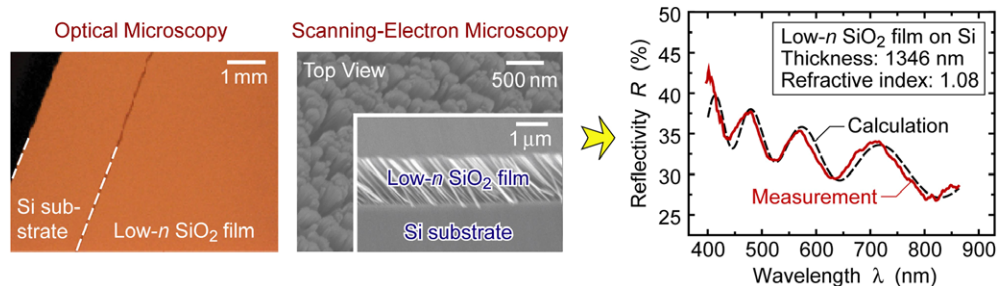


Figure 21. Optical micrograph and scanning-electron micrograph of low- n SiO_2 nano-rod film deposited on a Si substrate. The reflectance measurement reveals an extremely low refractive index of $n = 1.08$.

To produce a low- n material, dielectric materials are used as the evaporation source. During deposition, the vapour is well controlled to have small and constant vapour flux. A scanning-electron micrograph of a SiO_2 nano-rod layer grown by oblique-angle deposition on a Si substrate is shown in figure 20. Inspection of the micrograph indicates that the nano-rods are uniformly distributed with a tilt angle, θ_t . Since the film is deposited by evaporation, the controllability of film thickness is excellent and very suitable for deposition of quarter-wavelength thick optical films.

4.3. Low-refractive-index SiO_2

Optical films consisting of an array of SiO_2 nano-rods with a refractive index as low as $n = 1.08$ were demonstrated by Xi *et al* in 2005 and 2006 and are shown to have viable optical properties thereby making them very desirable for many applications [48, 49]. The optical films are fabricated by electron-beam evaporation of SiO_2 onto a substrate that is tilted so that vapour flux has an incident tilt angle of 85° with respect to the substrate-normal direction. The evaporation source material is pure SiO_2 granules. During the deposition, the chamber pressure is 2×10^{-6} Torr, and the deposition rate is 0.5 nm s^{-1} . As a result, the growth direction of the nano-rods is about 30° – 45° with respect to the surface normal of the sample.

The optical micrograph of a thick low- n SiO_2 nano-rod film deposited on a Si substrate is shown in figure 21 along with scanning-electron micrographs showing the top view and the cross-section view of the film. The optical micrograph reveals a smooth specular surface with no indication of scattering. The scanning-electron micrograph of cross-sectional view clearly shows the array of tilted SiO_2 nano-rods. Both the gaps between the SiO_2 nano-rods and the nano-rod diameters are $< 50 \text{ nm}$, i.e. much smaller than the wavelength of visible light, thereby limiting optical scattering.

The experimental reflectivity of a low- n SiO_2 nano-rod film on a Si substrate as a function of wavelength is shown in figure 21. The reflectivity reveals periodic interference oscillations. Analysis of the thin-film interference oscillations reveals that the film has a refractive index of 1.08 and a thickness of $1.35 \mu\text{m}$. These values were confirmed by both ellipsometry measurements and thin-film thickness measurements using scanning-electron microscopy. Furthermore, the films were found to be fully transparent with an optical absorption below the detection limit.

Figure 22 shows the scanning-electron micrograph of a cross-section view of the SiO_2 nano-rod layer ($h = 150 \text{ nm}$) on a Si substrate. The SiO_2 nano-rods are uniformly distributed with a tilt angle of $\theta_t = 45^\circ$. The gap between the SiO_2 nano-rods is less than 50 nm ,

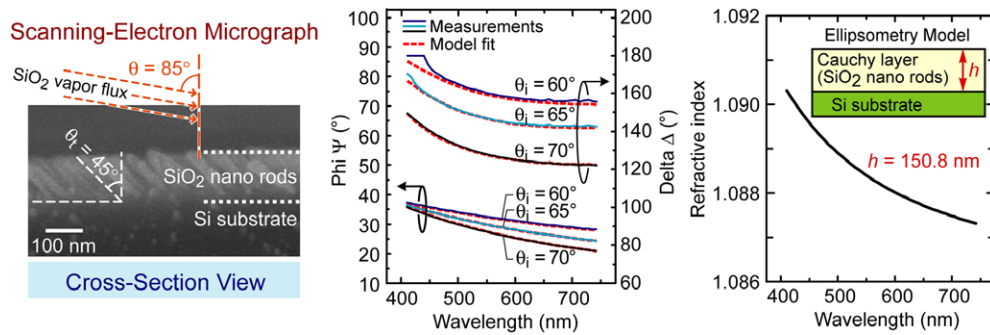


Figure 22. Scanning-electron micrograph of cross-section view for the SiO₂ nano-rod film with thickness $h = 150$ nm. The incidence angle of vapour flux is $\theta = 85^\circ$.

much smaller than the wavelength of visible light, and hence sufficiently small to limit optical scattering.

The refractive index of this thin film is independently measured by ellipsometry [50, 51] using multiple beam incident angles of 60° , 65° and 70° . The ellipsometry raw data, Ψ and Δ , and the model fit versus wavelength are shown in figure 22. The ellipsometry model assumes a Cauchy-type layer on a Si substrate. The model fits the measurement data very well with a mean-square-error of 4.92. The refractive index versus wavelength is also shown in figure 22. Within the visible spectrum, the refractive index of the SiO₂ nano-rod layer is extremely low. The thickness of the SiO₂ nano-rod layer, determined from the ellipsometry measurement, is $h = 150.8$ nm, confirming the thickness obtained by scanning-electron microscopy. Oblique-angle deposited films have been reported to be optically anisotropic [52], that is, the refractive index varies as a function of incident angle and polarization. However, no pronounced optical anisotropy is found in our thin SiO₂ nano-rod film, probably due to high porosity. Generally, the refractive index of a porous material is related to the degree of porosity and the refractive index of the non-porous dense material. Assuming a linear dependence, a refractive index of 1.08 implies a porosity of 82.6%.

4.4. Optical multilayer structure with low-refractive-index SiO₂ thin film

SiO₂ nano-rod layers fabricated by oblique-angle electron-beam deposition at an incident angle of 85° have a very low refractive index, namely $n_{\text{low}} \approx 1.08$. To demonstrate the viability of the SiO₂ nano-rod films for use in multilayer optical components, a single-pair DBR with a Si/SiO₂ nano-rod layer has been fabricated. Figure 23 shows the fabrication steps of a single-pair DBR. In order to avoid the filling of electron-beam-evaporated Si into the openings between SiO₂ nano rods, a very thin (20 nm) sealant layer is formed on the top surface of the SiO₂ nano-rod layer. The deposition conditions of the sealant layer are the same as those for the SiO₂ nano-rod layer except that the vapour flux incidence angle is $\theta = -45^\circ$, which changes the nano-rod growth direction. After the sealant layer, a 41 nm-thick Si layer is deposited at normal incidence by electron-beam evaporation. The scanning-electron micrograph of the Si/low- n SiO₂ DBR is also shown in figure 23. The cross-section view clearly shows that the electron-beam-deposited Si is lying on the sealant layer of the SiO₂ nano-rod layer, forming a sharp interface between them. Although the top view of the DBR shows some texture, the feature size is much smaller than the wavelength of visible light. The atomic-force micrograph of the surface for the DBR, shown in figure 24, has a root-mean-square surface roughness of 5.2 nm.

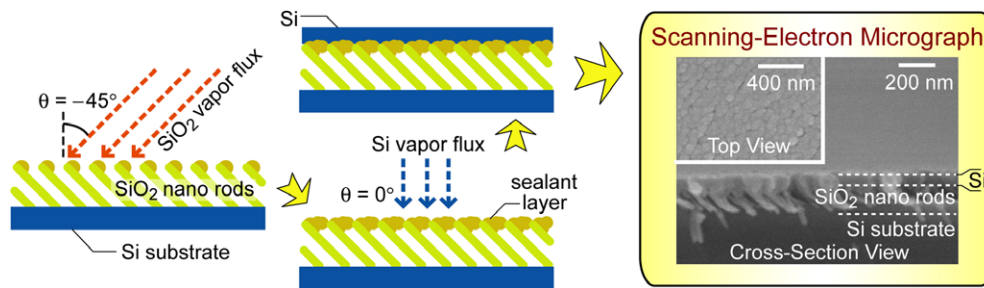


Figure 23. Fabrication steps for single-pair DBR incorporating a low- n SiO₂ nano-rod layer with a sealant layer. The scanning-electron micrograph shows that the Si layer is stably lying on the low- n SiO₂ layer. The top surface of the DBR is optically smooth although some surface texture is formed.

Atomic-Force Microscopy

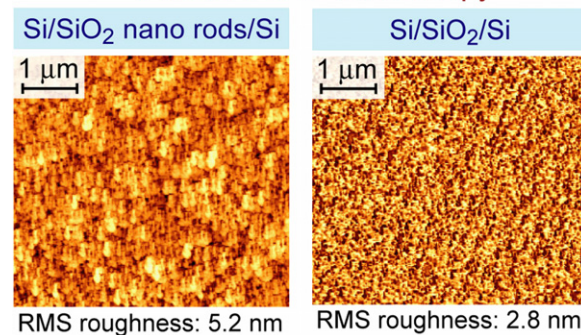


Figure 24. Atomic-force micrograph of the surface of a Si/low- n SiO₂ single-pair DBR and a reference Si/dense SiO₂ single-pair DBR. The measurement area is $5\ \mu\text{m} \times 5\ \mu\text{m}$.

For comparison, a single-pair DBR with Si/dense SiO₂ is deposited on a Si substrate by electron-beam evaporation using normal incidence evaporation. The thickness of dense SiO₂ is 107 nm to guarantee that the optical thickness of the dense SiO₂ and the low- n SiO₂ layer are equal. The thickness of Si is 41.0 nm. The atomic-force micrograph of Si/dense SiO₂ DBR, shown in figure 24, has a root-mean-square surface roughness of 2.8 nm.

The reflectivity at normal incidence of the DBRs is measured for visible and near infrared wavelengths. Both the measured and calculated reflection spectrum is plotted on the left-hand side of figure 25. In the calculation, a refractive index of 1.08 and 1.46 is used for the low- n SiO₂ and dense SiO₂ layer, respectively. Electron-beam deposited Si has a refractive index of $2.94 + 0.110i$ at the wavelength of 632.8 nm. Inspection of figure 25 reveals that the normal-incidence reflectivity is clearly enhanced for the DBR with the low- n SiO₂ nano-rod layer compared with the DBR using the dense SiO₂. The measured peak reflectivity of the Si/low- n SiO₂ DBR is $R = 78.9\%$. The measured peak reflectivity of the Si/dense SiO₂ DBR is $R = 72.0\%$. The measurement data matches the calculations very well. The increase in reflectivity shows the huge potential of low- n thin films for optical coatings, reflectors, photonic crystals and solid-state lighting devices.

The angular dependence of the reflectivity of the single-pair DBR structure is measured using a He-Ne laser source. The results are also shown in figure 25. Inspection of the figure clearly reveals that the normal-incidence reflectivity is enhanced for the DBR using low- n SiO₂

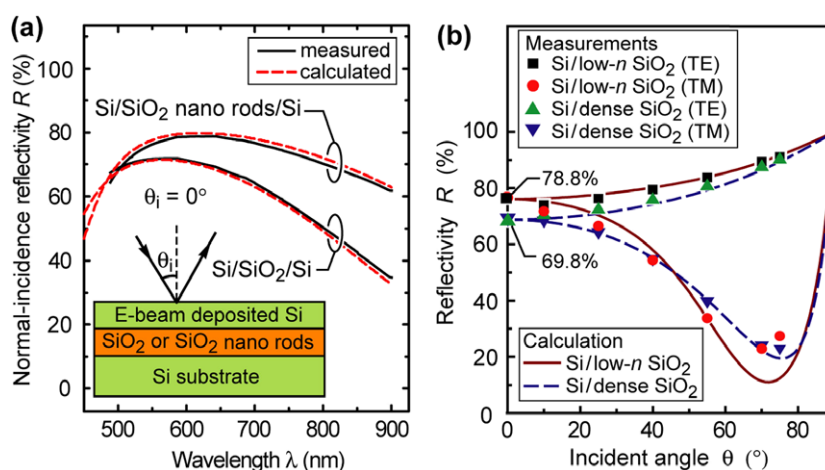


Figure 25. (a) Normal-incidence and (b) angular reflectivity of Si/low- n SiO₂ single-pair DBR and a Si/dense SiO₂ single-pair DBR on a Si substrate. The angular dependent reflectivity is measured for both the TE and TM polarizations at a wavelength of 632.8 nm.

nano-rod layer compared with the DBR using the dense SiO₂. The experimental near-normal-incidence reflectivity is 78.8% and 69.8% for the DBR using the low- n and dense SiO₂ films, respectively. The experimental results are in excellent agreement with the calculations.

5. Conclusions

In conclusion, the benefits of solid-state lighting in terms of energy savings, reduction of environmental pollution and new functionalities are reviewed. Solid-state light sources are in the process of profoundly changing the way we generate light for general lighting and other applications. In contrast to conventional lighting sources, solid-state sources have the potential to create light with unit power efficiency. Furthermore, the properties of light emitted by solid-state sources, such as spectral composition, polarization, colour temperature, temporal modulation and far-field emission pattern, can be controlled to a degree that is impossible with conventional light sources such as incandescent and fluorescent lamps. The implications are enormous and, as a consequence, many positive developments are to be expected including a reduction in global energy consumption, reduction of global-warming-gas and pollutant emissions and a multitude of new functionalities benefiting numerous applications. The impact of solid-state lighting technology on energy consumption and the environment is assessed in terms of a detailed yet fully transparent quantitative analysis. The impact on emerging application fields that make use of the controllability afforded by solid-state sources is discussed as well.

We also reviewed key technical areas that fuel continued progress in solid-state lighting. Specifically, we reviewed the use of novel phosphor distributions, namely *remote phosphor distributions*, in white LED lamps and show that remote phosphor distributions have higher efficiency and potentially higher reliability. We also reviewed the development of reflectors in LEDs with emphasis on ‘perfect’ reflectors, i.e. reflectors with highly reflective omnidirectional characteristics. Finally, we discussed a new class of thin-film materials with an unprecedented low refractive index. Such low- n materials may strongly contribute to continuous progress in solid-state lighting.

Acknowledgments

The authors gratefully acknowledge support by the National Science Foundation, Army Research Office, Department of Energy, Sandia National Laboratory, New York State, Samsung Corporation and Crystal IS Corporation. The authors also acknowledge useful discussions with Professors William N Gill, Shawn Y Lin, Toh-Ming Lu and Joel L Plawsky.

References

- [1] Schubert E F and Kim J K 2005 Solid-state light sources getting smart *Science* **308** 1274
- [2] Schubert E F 2006 *Light-Emitting Diodes* 2nd edn (Cambridge, UK: Cambridge University Press)
- [3] United States Energy Information Administration 2004 *Annual energy review* Report No. DOE/EIA-0384 and <http://www.eia.doe.gov/emeu/aer/elect.html>
- [4] Bergh A, Craford M G, Duggal A and Haitz R 2001 The promise and challenge of solid-state lighting *Phys. Today* **55** 44 42
- [5] US Department of Energy (DOE) 2006 *Solid-State Lighting Research and Development Portfolio; Multi-year program plan FY'07-FY'12* (Chicago: Navigant Consulting)
- [6] United States Energy Information Administration 1998 *25th Anniversary of the 1973 Oil Embargo* <http://www.eia.doe.gov/emeu/25opec/sld000.htm>
- [7] Genet M, Villette S, Bourg-Heckly G and Loiseau S 2003 Development of a novel optical biopsy system combining optical-fiber reflectance confocal imaging and confocal autofluorescence spectroscopy *European Conf. on Biomedical Optics (Munich, Germany, June 2003)*
- [8] Kutuza I B, Pozhar V E and Pustovoi V I 2003 AOTF-based imaging spectrometers for research of small-size biological objects *Proc. SPIE* **5143** 165
- [9] Brainard G C, Hanifin J P, Greeson J M, Byrne B, Glickman G, Gerner E and Rollag M D 2001 Action spectrum for melatonin regulation in humans: evidence for a novel circadian photoreceptor *J. Neurosci.* **21** 6405
- [10] Blask D E, Dauchy R T, Sauer L A, Krause J A, Brainard G C 2003 Growth and fatty acid metabolism of human breast cancer (MCF-7) xenografts in nude rats: impact of constant light-induced nocturnal melatonin suppression *Breast Cancer Res. Treat.* **79** 313
- [11] Dowling J E 1987 *The Retina* (Cambridge, MA: Harvard University Press)
- [12] Carruthers J B 2002 *Wireless infrared communications* *Wiley Encyclopedia of Telecommunications* ed J G Proakis (New York: Wiley)
- [13] Nhut D T, Takamura T, Watanabe H, Okamoto K and Tanaka M 2003 Responses of strawberry plantlets cultured in vitro under super-bright red and blue light-emitting diodes (LEDs) *Plant Cell Tissue Organ Culture* **73** 43
- Jao R C and Fang W 2003 An adjustable light source for photo-phyto related research and young plant production *Appl. Eng. Agric.* **19** 601
- [14] Chigrinov V G 1999 *Electrooptic Effects in Liquid Crystal Materials* (Norwood, MA: Artech House)
- [15] Nakamura S and Fasol G 1997 *The Blue Laser Diode: GaN Based Light Emitters and Lasers* (Berlin: Springer)
- [16] Mueller-Mach R, Mueller G O and Krames M R 2004 Phosphor materials and combinations for illumination graded white pcLED *Third Int. Conf. Solid State Lighting (San Diego CA, August 2003)* *Proc. SPIE* **5187** 115
- [17] Kim J K, Luo H, Schubert E F, Cho J, Sone C and Park Y 2005 Strongly enhanced phosphor efficiency in GaInN white light-emitting diodes using remote phosphor configuration and diffuse reflector cup *Japan. J. Appl. Phys.—Express Lett.* **44** L 649
- [18] Luo H, Kim J K, Schubert E F, Cho J, Sone C and Park Y 2005 Analysis of high-power packages for phosphor-based white-light-emitting diodes *Appl. Phys. Lett.* **86** 243505
- [19] Kim J K, Gessmann T, Luo H and Schubert E F 2004 GaInN light-emitting diodes with RuO₂/SiO₂/Ag omnidirectional reflector *Appl. Phys. Lett.* **84** 4508
- [20] Rayleigh L 1912 The problem of the whispering gallery *Sci. Papers* **5** 617
- [21] Luo H, Kim J K, Xi Y, Schubert E F, Cho J, Sone C and Park Y 2006 Trapped whispering-gallery optical modes in white light-emitting diode lamps with remote phosphor *Appl. Phys. Lett.* **89** 041125
- [22] Schade H and Smith Z E 1985 Mie scattering and rough surfaces *Appl. Opt.* **24** 3221
- [23] Xi Y, Li X, Mont F, Gessmann Th, Luo H and Schubert E F 2006 Quantitative assessment of diffusivity and specularity of surface-textured reflectors for light extraction in light-emitting diodes *J. Vac. Sci. Technol. A* **24** 1627
- [24] Gessmann T, Schubert E F, Graff J W, Streubel K and Karnutsch C 2003 Omnidirectional reflective contacts for light-emitting diode *IEEE Electron Device Lett.* **24** 683

- [25] Gessmann T and Schubert E F 2004 High-efficiency AlGaInP light-emitting diodes for solid-state lighting applications *J. Appl. Phys.* **95** 2203
- [26] Kim J K, Gessmann T, Luo H and Schubert E F 2004 GaInN light-emitting diodes with RuO₂/SiO₂/Ag omnidirectional reflector *Appl. Phys. Lett.* **84** 4508
- [27] Born M and Wolf E 1987 *Principle of Optics* 6th edn (Oxford: Pergamon) p 62
- [28] Kim J K, Gessmann T, Schubert E F, Xi J-Q, Luo H, Cho J, Sone C, and Park Y 2004 GaInN light-emitting diodes with conductive omnidirectional reflector having a low-refractive-index indium–tin oxide *Appl. Phys. Lett.* **88** 013501
- [29] Gessmann T, Li Y-L, Schubert E F, Graff J W and Sheu J K 2003 GaInN light-emitting diodes with omnidirectional reflectors *Proc. SPIE* **4996** 26
- [30] Song J-O, Leem D-S, Kwak J S, Nam O H, Park Y, Seong T-Y 2003 Low-resistance and highly-reflective Zn–Ni solid solution/Ag ohmic contacts for flip-chip light-emitting diodes *Appl. Phys. Lett.* **83** 4990
- [31] Krames M R *et al* 1999 High-power truncated-inverted-pyramid (Al_xGa_{1-x})_{0.5}In_{0.5}P/GaP light-emitting diodes exhibiting >50 external quantum efficiency *Appl. Phys. Lett.* **75** 2365
- [32] Gardner N F, Chui H C, Chen E I, Krames M R, Huang J-W, Kish F A, Kocot C P, Tan T S and Moll N 1999 1.4× improvement in transparent substrate light-emitting diodes (Al_xGa_{1-x})_{0.5}In_{0.5}P/GaP with thin (<200 nm) active regions *Appl. Phys. Lett.* **74** 2230
- [33] Streubel K, Rapp S, André J and Chitica N 1996 1.26 μm vertical cavity laser with two InP/air-gap reflectors *Electron. Lett.* **32** 1369
- [34] Ho S-T, McCall S L, Slusher R E, Pfeiffer L N, West K W, Levi A F J, Blonder G E and Jewell J L 1990 High index contrast mirrors for optical microcavities *Appl. Phys. Lett.* **57** 1387
- [35] Temelkuran B, Hart S D, Benoit G, Joannopoulos J D and Fink Y 2002 Wavelength-scalable hollow optical fibres with large photonic bandgaps for CO₂ laser transmission *Nature* **420** 650
- [36] Xi J-Q, Ojha M, Cho W, Plawsky J L, Gill W N, Gessmann T and Schubert E F 2005 Omnidirectional reflector using nanoporous SiO₂ as a low-refractive-index material *Opt. Lett.* **30** 1518
- [37] Xi J-Q, Ojha M, Plawsky J L, Gill W N, Kim J K and Schubert E F 2005 Internal high reflectivity omnidirectional reflectors *Appl. Phys. Lett.* **87** 031111
- [38] Nitta S V, Pisupatti V, Jain A, Wayner P C Jr, Gill W N and Plawsky J L 1999 Surface modified spin-on xerogel films as interlayer dielectrics *J. Vac. Sci. Technol. B* **17** 205
- [39] Jain A, Rogojevic S, Ponoth S, Agarwal N, Matthew I, Gill W N, Persans P, Tomozawa M, Plawsky J L and Simonnyi E 2001 Porous silica materials as low-*k* dielectrics for electronic and optical interconnects *Thin Solid Films* **398–399** 513
- [40] Jain A, Rogojevic S, Ponoth S, Gill W N, Plawsky J L, Simonyi E, Chen S T and Ho P S 2002 Processing dependent thermal conductivity of nanoporous silica xerogel films *J. Appl. Phys.* **91** 3275
- [41] Gill W N, Plawsky J L and Xi J Q 2005 personal communication
- [42] Holland L 1953 The effect of vapor incidence on the structure of evaporated aluminum films *J. Opt. Soc. Am.* **43** 376
- [43] Lakhtakia A and Messier R 2005 *Sculptured Thin Films: Nanoengineered Morphology and Optics* (Washington: SPIE)
- [44] Robbie K, Friedrich L J, Dew S K, Smy T and Brett M J 1995 Fabrication of thin films with highly porous microstructures *J. Vac. Sci. Technol. A* **13** 1032
- [45] Abelmann L and Lodder C 1997 Oblique evaporation and surface diffusion *Thin Solid Films* **305** 1
- [46] Robbie K and Brett M J 1997 Sculptured thin films and glancing angle deposition: growth mechanics and applications *J. Vac. Sci. Technol. A* **15** 1460
- [47] Vick D, Friedrich L J, Dew S K, Brett M J, Robbie K, Seto M and Smy T 1999 Self-shadowing and surface diffusion effects in obliquely deposited thin films *Thin Solid Films* **339** 88
- [48] Xi J-Q, Kim J K and Schubert E F 2005 Silica nanorod-array films with very low refractive indices *Nano Lett.* **5** 1385
- [49] Xi J-Q, Kim J K, Schubert E F, Ye D, Lu T-M and Lin S-Y 2006 Very low-refractive-index optical thin films consisting of an array of SiO₂ nanorods *Opt. Lett.* **31** 601
- [50] Woollam J A, Johs B, Herzinger C M, Hilfiker J, Synowicki R and Bungay C L 1999 Overview of variable angle spectroscopic ellipsometry (VASE): I. Basic theory and typical applications *Crit. Rev. Opt. Sci. Technol.* **CR72** 3
- [51] Johs B, Woollam J A, Herzinger C M, Hilfiker J, Synowicki R and Bungay C L 1999 Overview of Variable Angle Spectroscopic Ellipsometry (VASE): II. Advanced applications *Crit. Rev. Opt. Sci. Technol.* **CR72** 29
- [52] Kaminska K and Robbie K 2004 Birefringent omnidirectional reflector *Appl. Opt.* **43** 1570